The Meteoritical Society

Meteoritics & Planetary Science 53, Nr 5, 984–1005 (2018)
doi: 10.1111/maps.13040

Cooling rates of type I chondrules from Renazzo: Implications for chondrule formation

Noël CHAUMARD[1,4*], Munir HUMAYUN[2], Brigitte ZANDA[1], and Roger H. HEWINS[1,3]

[1]Institut de Minéralogie, de Physique des Matériaux et de Cosmochimie, Sorbonne Universités, Muséum national d'histoire naturelle, UPMC Université Paris 06, UMR CNRS 7590, IRD, UMR 206, CP 52, 57 rue Cuvier, 75231 Paris Cedex 05, France
[2]Department of Earth, Ocean & Atmospheric Science, and National High Magnetic Field Laboratory, Florida State University, Tallahassee, Florida 32310, USA
[3]Department of Earth & Planetary Sciences, Rutgers University, Piscataway, New Jersey 08855, USA
[4]Department of Geoscience, WiscSIMS, University of Wisconsin-Madison, 1215 W. Dayton Street, Madison, Wisconsin 53706–1632, USA
*Corresponding author. E-mail: chaumard@wisc.edu

(Received 13 July 2016; revision accepted 28 November 2017)

Abstract–Cooling rates are one of the few fundamental constraints on models of chondrule formation. In this study, we used Cu and Ga diffusion profiles in metal grains to determine the cooling rates of type I chondrules in the Renazzo CR2 chondrite. To improve previous estimations of cooling rates obtained using this method, we used CT scanning and serial polishing of our sections to analyze equatorial sections of large metal grains. Through the cores of these metal grains situated at the surface of chondrules, the cooling rates calculated range from 21 to 86 K h^{-1} for a peak temperature $T_p \sim 1623$–1673 K. A metal grain embedded in the core of a chondrule exhibits a cooling rate of 1.2 K h^{-1} at a $T_p \sim 1573$ K. We also measured Cu-Ga diffusion profiles from nonequatorial sections of metal grains and calculated a lower range of cooling rates of 15–69 K h^{-1} for $T_p \sim 1473$–1603 K compared to our results from equatorial sections. The high cooling rates inferred from the lightning model (several thousand K h^{-1}) are clearly at odds with the values obtained in this work. The X-wind model predicts cooling rates (~6–10 K h^{-1}) lower than most of our results. The cooling rates calculated here are in close agreement with those inferred from shock wave models, in particular for temperatures at which olivine crystallizes (from ~10 to several hundreds K h^{-1} between 1900 and 1500 K). However, the chemical compositions of metal grains in Renazzo are consistent with the splashing model, in which a spray of metal droplets originated from a partially molten planetesimal. Volatile siderophile element depletion is explained by evaporation before metal was engulfed within silicate droplets. Liquid metal isolated from the liquid silicate crystallized during cooling, reacted with the ambient gas, and then re-accreted within partially molten chondrules.

INTRODUCTION

Chondrules are important components of carbonaceous chondrites (CCs) (e.g., Zanda 2004). Since the recognition of the igneous texture of chondrules by Sorby (1877), numerous heating mechanisms have been proposed for chondrule formation, which have been extensively discussed and reviewed (e.g., Connolly et al. 2006; Desch et al. 2012). The most popular models involve either the Sun as the heat source for chondrule formation, i.e., the X-wind model (e.g., Shu et al. 1996, 2001), or high-temperature events that took place in the nebular gas. The latter includes the lightning models (e.g., Pilipp et al. 1998; Desch and Cuzzi 2000), planetesimal bow shocks (Hood 1998; Weidenschilling et al. 1998; Ciesla et al. 2004; Hood et al. 2005, 2009), and shock fronts possibly driven by gravitational instabilities passing through the gas (e.g., Desch and Connolly 2002; Morris and Desch 2010). Alternative models, such as collision between planetesimals generating melt droplets, have also been proposed for the formation of chondrules (e.g., Sanders 1996; Sanders and Taylor 2005; Sanders and Scott 2012) and modeled by Asphaug et al. (2011) and Johnson et al. (2015). This origin of chondrules in impact-generated plumes is invoked to explain the high dust/gas ratio and the high total pressure and Na partial pressure required for Na retention in chondrules (Alexander et al. 2008; Alexander and Ebel 2012; Fedkin et al. 2012; Hewins et al. 2012; Fedkin and Grossman 2013).

One of the constraints on the formation of chondrules that petrological studies have provided is an estimate of the cooling rate experienced by chondrules. The mechanisms for chondrule formation discussed above were primarily proposed on the basis of cooling rates estimated for type II (oxidized) chondrules, either those inferred from crystallization experiments that matched observed textures or from olivine zoning data (Jones 1990; Jones and Lofgren 1993; Lofgren 1996; Hewins et al. 2005) or diffusion modeling of zoning profiles in olivine (Hewins et al. 2009; Miyamoto et al. 2009). Although type II chondrules are dominant in ordinary chondrites (OCs), chondrules in enstatite and CCs are predominantly type I (e.g., Zanda et al. 2006; Jones 2012). These two classes of chondrites are dominated by type I (reduced) chondrules. Compared to type II chondrules, fewer experiments have been done on type I compositions, and forsteritic crystals are almost unzoned in type I chondrules (Radomsky and Hewins 1990; Hewins 1997; Wick and Jones 2012) limiting the tools with which to determine their cooling rates. Thus, using other methods, in particular those based on in situ measurements of cooling rates on type I chondrules, is of utmost importance to provide additional constraints on chondrule formation. Weinbruch and Müller (1995) and Cuvillier et al. (2014) reported cooling rates of type I chondrules from the systematics of exsolution of pigeonite from diopside, while Humayun (2012) estimated cooling rates from diffusion profiles of volatile elements in metal grains exposed at the surfaces of type I chondrules. Humayun (2012) measured Cu and Ga zoning profiles by laser ablation inductively coupled plasma–mass spectrometer (LA-ICP-MS) through metal lumps attached to type I chondrules in the Acfer 097 CR2 chondrite. The author used the mutual diffusivities of Cu and Ga to infer the temperature at which the zoning profiles formed and the cooling rates associated, from the correlation of Cu versus Ga. In the study conducted by Humayun (2012), an important source of uncertainty to the cooling rates arose from the random orientation of metal grains exposed in the sections. Indeed, the cooling rates inferred from diffusion profiles passing through a nonequatorial plane are systematically underestimated.

Because metal (Fe-Ni alloy) is abundant in CR chondrites and is often in association with chondrules (e.g., Wood 1963; Weisberg et al. 1993), we decided to use the method developed by Humayun (2012) to obtain cooling rates from the Renazzo CR2 chondrites. To improve on the work of Humayun (2012) and provide additional constraints on the heating mechanisms that prevailed in the protoplanetary disk, we avoided the underestimation of the cooling rates by using equatorial sections. Indeed, profiles measured through nonequatorial sections display gentler chemical gradients than radial chemical profiles passing through the core of the lumps. Calculation inferred from diffusion profiles not passing through an equatorial plane will thus give underestimated cooling rates. So, we measured radial Cu and Ga zoning profiles by LA-ICP-MS through large metal lumps. These metal lumps were previously identified by X-ray computed tomography (CT) and subsequently sectioned to expose their equatorial sections at the polished surface of our samples. On the basis of devolatilization/recondensation processes consistent with the major and trace siderophile element abundances in metal grains from CR chondrites (Kong and Palme 1999; Kong et al. 1999; Humayun et al. 2002, 2010; Zanda et al. 2002), it was proposed that liquid metal exposed to ambient vapor was partially depleted in volatile elements such as Cu, Ga, Ge, and Au by evaporation during the chondrule melting events, subsequently recondensed at the exterior of the solid metal grains and diffused inward (Kong et al. 1999; Connolly et al. 2001; Hewins and Zanda 2012; Humayun 2012). In this study, we report the analyses of Cu and Ga diffusion profiles to provide cooling rate constraints on the high-temperature event that formed type I chondrules and their solid-state history, and use this evidence to test the predictions of astrophysical models of chondrule formation.

ANALYTICAL METHODS AND TECHNIQUES

To obtain 3-D information and to enable measurements of chemical profiles through the centers of metal grains, we imaged a fragment of Renazzo by CT scanning using a v|tome|x 240L from GE Sensing & Inspection Technologies Phoenix X|Ray at the Muséum national d'Histoire naturelle (MNHN, Paris). This fragment of Renazzo was scanned using a 100 kV acceleration voltage and 230 μA current. X-ray transmission was recorded on a 1024^2 pixel detector panel (pixel size: 200×200 μm) and the scans resulted in a stack of 1953 slices with a resolution of ~0.10 μm (voxel size). Data reduction was carried out using the Avizo and Fiji imaging software and we used a computer reconstruction, which consists of cubic voxels, to locate with precision type I chondrules with large (>300 μm) metal lumps. We used this stack of CT-scan images of Renazzo to define planes containing as many equatorial sections of large metal grains as possible. We thus cut two fragments of Renazzo parallel to surfaces containing the equatorial planes of a maximum of large metal grains. We then embedded the two sections in epoxy resin for further analyses. Finally, we ground these two sections until the equatorial planes of the large selected metal grains corresponded to the polished surface of our sample (Fig. 1). The stack of CT-scan images was used to check if the equatorial plane of each large metal grain selected was reached. Additional metal grains, for which a nonequatorial section was exposed at the polished surfaces, were also analyzed.

Secondary electron (SE) and backscattered electron (BSE) imaging were performed at the Institut de Minéralogie, de Physique des Matériaux et de Cosmochimie (IMPMC, Université Pierre et Marie Curie—Muséum national d'Histoire naturelle, Paris) using a Tescan VEGA II LSU scanning electron microscope (SEM) equipped with a Bruker SD^3 energy-dispersive X-ray spectrometer (EDS) for the acquisition of compositional maps. In order to investigate the distribution of major elements in silicates, metal, and sulfides (e.g., Fe, Mg, Ni, S, etc.), we acquired elemental maps by EDS using an accelerating voltage of 15 keV. RGB compositional maps have a resolution of ~1.7 μm/pixel.

Laser scan profiles across metal lumps were measured by LA-ICP-MS using a New Wave™ UP193FX ArF excimer laser system coupled to a Thermo Element XR™ ICP-MS at the Plasma Analytical Facility at the National High Magnetic Field Laboratory, Florida State University. The main details of the instrumentation and methodology used here were described previously (Campbell and Humayun 1999; Humayun et al. 2007; Gaboardi and Humayun 2009; Humayun 2012). Laser scan profiles were measured using a 15 μm spot size, 5 μm s^{-1} speed, 50 Hz repetition rate, and 100% power output (1.55 GW cm^{-2}). The peaks ^{31}P, ^{34}S, ^{51}V, ^{53}Cr, ^{57}Fe, ^{59}Co, ^{60}Ni, ^{63}Cu, ^{66}Zn, ^{69} Ga, ^{74}Ge, ^{75}As, ^{95}Mo, ^{102}Ru, ^{103}Rh, ^{106}Pd, ^{120}Sn, ^{121}Sb, ^{184}W, ^{185}Re, ^{192}Os, ^{193}Ir, ^{195}Pt, and ^{197}Au were acquired in low mass resolving power (R = 400) and in Triple mode. Standards used were the North Chile (Filomena) IIA iron meteorite, the Hoba IVB iron meteorite, and NIST SRM 1263a steel. To obtain comparable results for comparison with Humayun (2012), we averaged a set of approximately five consecutive mass scans of the mass spectrum corresponding to approximately 15 μm of track length to improve the precision of the concentrations measured. This procedure is particularly useful for zoning profiles from equatorial lumps since cores are depleted in Cu and Ga with concentrations close to the detection limits, ~8 and ~0.7 ppm, respectively. Due to the low Cu and Ga contents measured in the cores of metal lumps, we did not use the parts of each zoning profile with concentrations close to the detection limits for thermometric estimations. This procedure avoids possible scattering in the calculated peak temperatures at which the diffusion profile began to be formed (T_p) and thus in the cooling rates. Each diffusion profile is characterized by a diffusion length-scale determined by numerically fitting an error function to the measured profiles of Cu using a MatLab routine.

To obtain precise compositions for even the most volatile elements and to compare with the bulk compositions determined from profiles, laser spots were measured in the metal lump 2C2 using a 50–100 μm spot size, 10 s dwell time, 50 Hz repetition rate, and 100% power output.

Profiles taken across grains were pushed as close to the edge of the metal as possible. Figures 2c and 3b show that a thin rim of sulfides that contain strong S enrichments at the very edge surrounds the metal grains. Since beam penetration of this sulfide rim is possible, each of the profiles was examined for Si and S abundances. Those analyses near the rim that contained Si and S above the blank levels were not used in the metal profiles. It is possible that this reduced the maximum value of the Cu and Ga abundances at the rims of the metal grains, but these analyses are too enriched in Cu to be useful in calculating cooling rates.

RESULTS

Petrographic Description of Chondrules and Metal Lumps

During this study, we investigated metal lumps either included in or attached to type IAB porphyritic chondrules (Figs. 2 and 3). Olivine is forsteritic ($Fo_{94.9–98.7}$; average $Fo_{97.2 \pm 1.2}$) and pyroxene is mainly present as large enstatite ($En_{95.0–97.4}Wo_{0.4–0.9}$; average $En_{96.4 \pm 0.7}$ $Wo_{0.7 \pm 0.2}$) grains. Most of the chondrules are mesostasis-rich and numerous diopside can be observed.

As shown in Figs. 2c and 3b, metal lumps situated at the borders of chondrules or located close to the chondrule/matrix interfaces are surrounded by rims of sulfides. These sulfides have sizes of a few microns and contain numerous cracks and fractures. They are inferred to be troilite and/or pyrrhotite based on EDS spectra. Contacts between metal grains are also

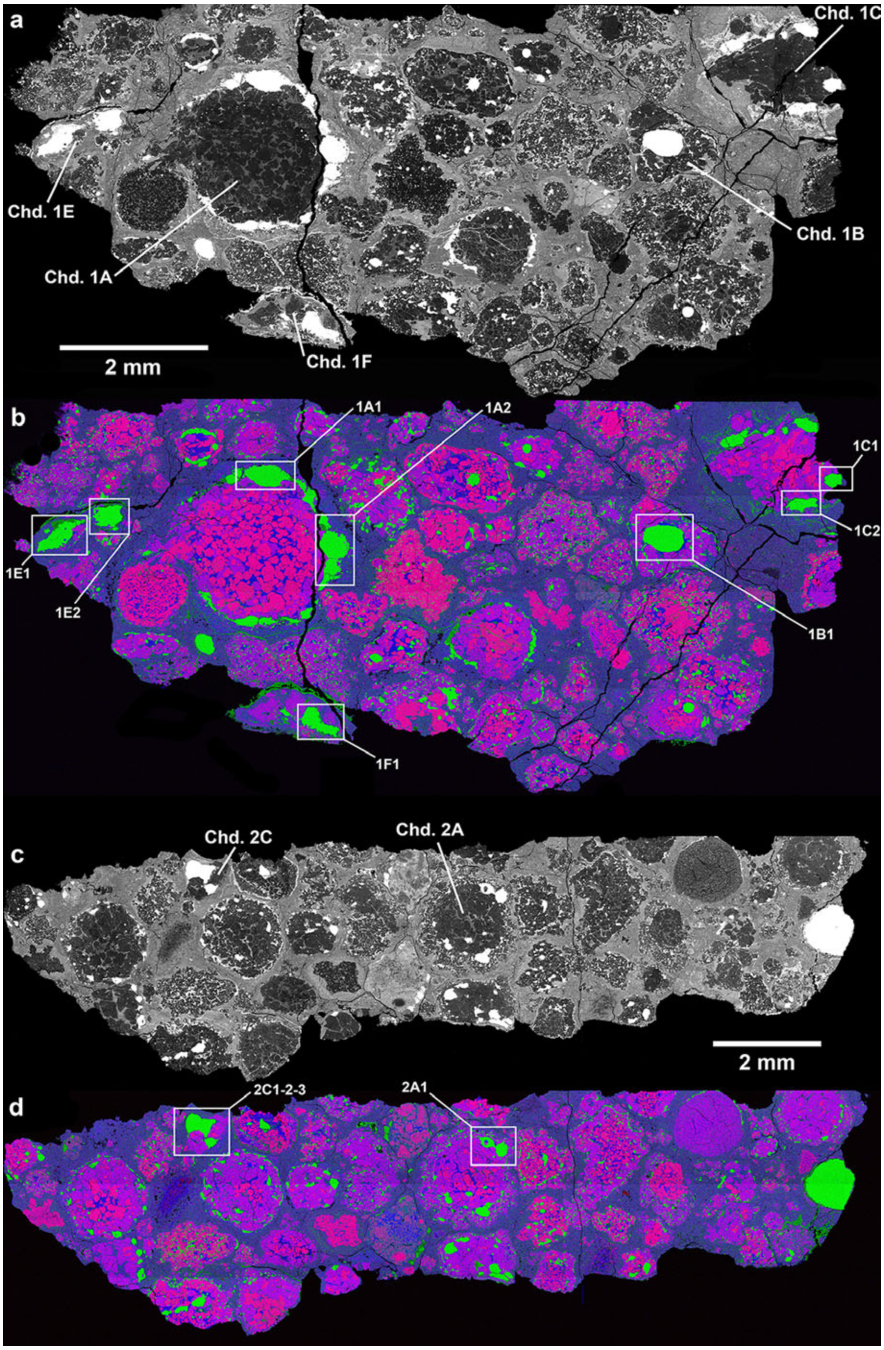

Fig. 1. BSE images of section 1 (a) and 2 (c) of Renazzo investigated. b and d) EDS compositional maps in RGB colors (R = Mg, G = Fe, B = Si) showing olivine (pink), pyroxene (purple), and metal (green). Matrix appears in blue. The chondrules investigated are labeled in the BSE images. Boxes in RGB maps indicate metal lumps analyzed by LA-ICP-MS. Metal lumps cut at an equatorial section: 1A1, 1A2, 1B1, and 2C1-2-3 (see Fig. 3a for the spatial and textural description of these three metal grains analyzed in the chondrule 2C). Metal grains cut close to an equatorial section: 1C2. Other metal grains were cut at a nonequatorial section. (Color figure can be viewed at wileyonlinelibrary.com.)

delimited by such Fe-rich sulfides (Fig. 3b). Metal lumps located within chondrules and with no contact with the matrix (checked in 3-D using CT scanning) do not display rims of Fe-rich sulfides (Fig. 2d).

When metal lumps are in contact with the matrix, they sometimes display lobed structures (Fig. 2a). In addition to the rim of Fe-rich sulfides, EDS data indicate that Fe-, Mg-, Al-rich oxides (spinels) and

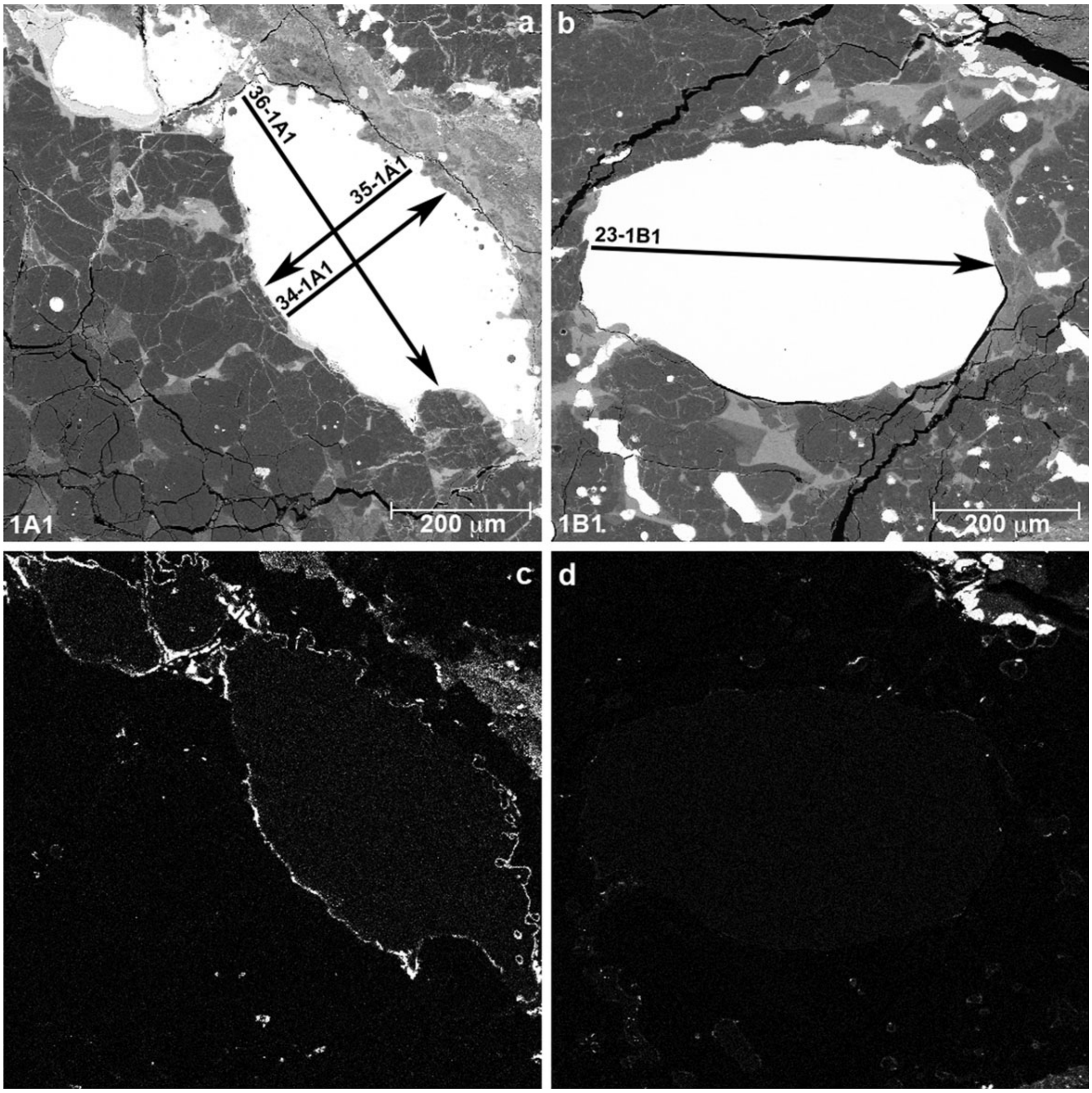

Fig. 2. a) BSE image of the 1A1 metal grain situated at the border of the 1A type I chondrule. The upper right border of this metal grain, which is in contact with the matrix, is characterized by the presence of lobed structures (some of them are indicated by dashed arrows) and displays numerous rounded inclusions of silicates. b) BSE image of the 1B1 metal grain situated in the interior of the 1B type I chondrule. See Fig. 1 for location. c, d) are EDS elemental maps of S corresponding to the area (a) and (b), respectively. White indicates high S contents that are concentrated at the edges of the 1A1 metal grain due to aqueous alteration corroding the grain rims.

hydroxides (possibly goethite) locally occur as rinds at the lobed border/matrix boundaries.

We also observed numerous rounded inclusions up to ~15 μm size located close to these lobed borders of metal grains (Fig. 2a). EDS spectra indicate that the smallest inclusions (<~5 μm) are either Si-rich or Cr,S-rich (sometimes euhedral, possibly daubréelite), while the largest ones may correspond to ferromagnesian silicates. Considering metal grains in three dimensions, the latter may correspond to the cross sections of lobed structures that are not in the plane of the polished surface.

Bulk Grain Abundances

We investigated 11 metal lumps attached to seven chondrules, for a total of 22 laser tracks. Nine tracks were taken through the equatorial sections of five metal grains from three chondrules with lengths ranging from ~190 to 500 μm. The other 13 tracks were taken through nonequatorial sections of six metal grains (~115–520 μm in length) representing four chondrules. The bulk grain abundances given in Table 1 were obtained by averaging each laser track measured along

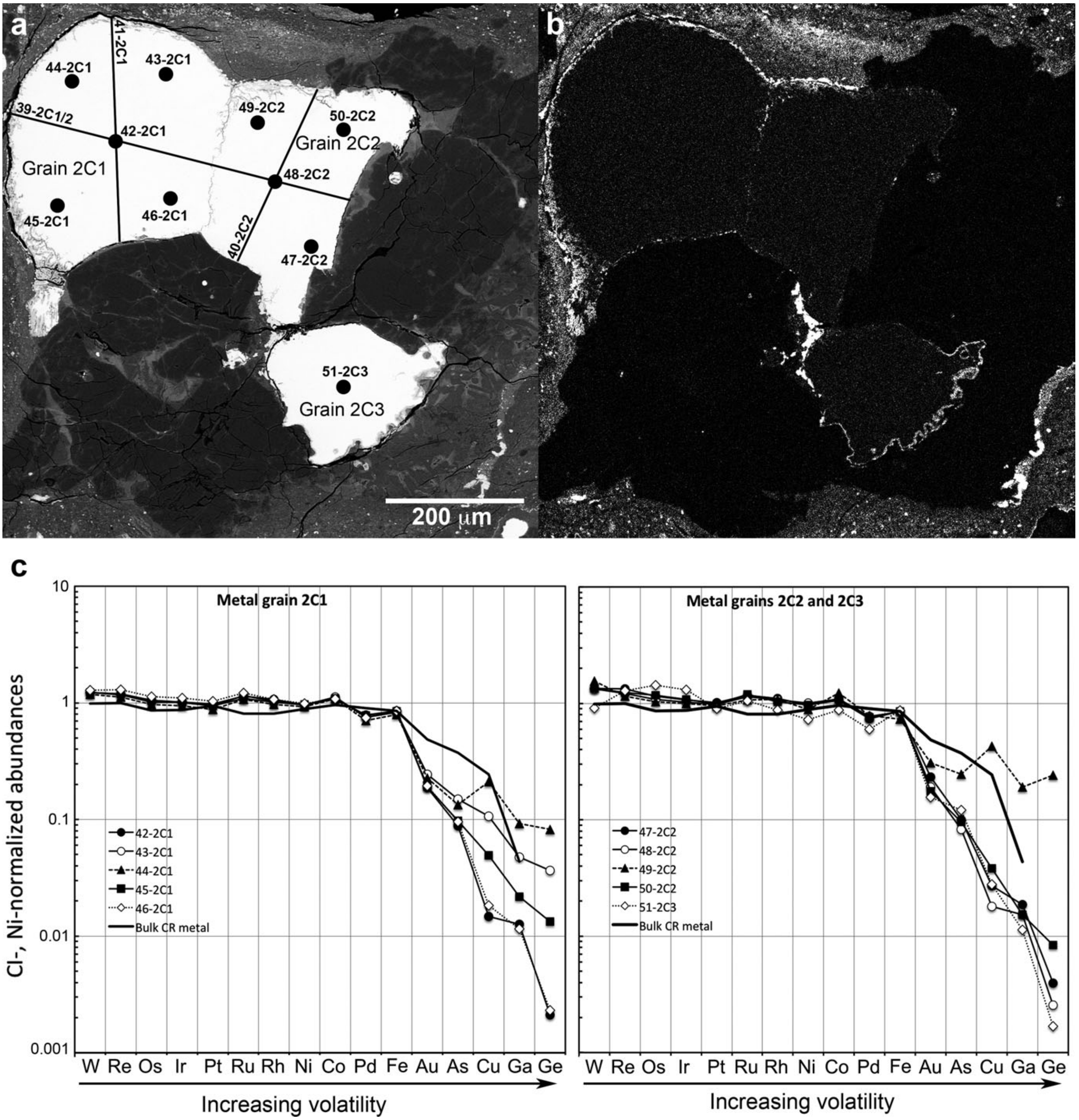

Fig. 3. a) BSE image and (b) EDS elemental map for S of the metal grains 2C1, 2C2, and 2C3 attached to the 2C type I chondrule in Renazzo (see Fig. 1 for location). a) The locations of all laser tracks (black lines) and spots (black circles) analyzed in these metal grains are shown on a BSE image. b) Sulfur X-ray map of the same chondrule as in (a) showing that the lower right border of grain 2C3 displays a lobed texture delimited by a rim of sulfides. c) Doubly normalized abundances (to CI chondrites and Ni) of siderophile elements for laser spots analyzed in the metal lumps shown as a function of increasing volatility. The composition of bulk CR metal (Kong et al. 1999) is shown for comparison.

either equatorial or nonequatorial sections of metal grains. These abundances, doubly normalized to CI chondrites and Ni, are presented in Figs. 3c and 4 as a function of volatility.

Table 1 shows that the Ni contents of equatorial sections (6.28 ± 0.21 wt%) are higher than those of nonequatorial sections (5.14 ± 0.32 wt%). The Co/Ni ratios range from 1.04 to 1.12 × CI for equatorial sections, and from 1.00 to 1.24 × CI for nonequatorial sections. Au contents range from 0.13 to 0.27 ppm in equatorial sections (excluding the 1B1 grain, which displays 0.43 ppm Au) and from 0.23 to 0.58 in nonequatorial sections. Au is roughly correlated with Cu, Ga, Ge, and Pd, and anticorrelated with Ni and Co.

The patterns of the bulk metal obtained from averaged laser tracks passing through equatorial sections display depletions in moderately volatile siderophile elements (As, Cu, Ga, and Ge) relative to CI abundances, from approximately 0.5 to 2 orders of magnitude (Fig. 4). These patterns are characterized by negative anomalies in Pd (0.63–0.76 × CI). Refractory elements are either roughly chondritic or depleted by up to ~0.5 orders of magnitude, and Os, Ir, and Pt are usually more depleted relative to the other refractory elements (e.g., W, Ru, and Rh).

Spot analyses performed using a 50 and 100 μm spot size from the equatorial section of the metal lumps associated with the chondrule 2C are given in Table 2. In the metal grains 2C1 and 2C2 (see Fig. 3a for location), refractory siderophiles are present in nearly chondritic abundances, close to that of bulk CR metal (Fig. 3c). These patterns are also characterized by a negative anomaly in Pd (0.63–0.76 × CI, with Pd contents ranging from 2.0 to 2.4 ppm) that is more depleted than Fe, an effect that cannot be attributed to volatility. Volatile siderophile elements are depleted relative to the bulk CR metal and chondritic abundances, by up to 2.5 orders of magnitude for Ge. Although depleted in volatile siderophile elements relative to CI chondrites and displaying a negative Pd anomaly, the core composition of metal grain 2C3 (see Fig. 3a for location) displays an enriched and fractionated (Re, Os, and Ir) refractory element pattern (Fig. 3c) characteristic of solid metal formed by fractional crystallization. The S, and to a lesser extent the Si contents, measured for the laser spots 43-2C1, 44-2C1, and 49-2C1 (Table 2) indicate contamination by silicates and/or altered materials since they are situated at the border of the lump 2C1 (Fig. 3). This contamination may have caused the slight enrichment in moderately volatile siderophile elements measured in these laser spots relative to the others (Fig. 3c).

The patterns of the bulk metal grains obtained from averaged laser tracks passing through nonequatorial sections are slightly less depleted in moderately volatile siderophile elements (As, Cu, Ga, and Ge) relative to CI abundances (by up to ~1.5 orders of magnitude) than patterns from equatorial sections (Fig. 4). These grains display depleted and fractionated refractory element patterns by up to an order of magnitude (Fig. 4), as also observed by Connolly et al. (2001) in metal grains associated with chondrules in CR2 chondrites. Metal grains analyzed through nonequatorial sections also display negative anomalies in Pd (0.60–0.86 × CI), with Pd contents ranging from 1.9 to 2.8 ppm.

Diffusion Profiles for Cu and Ga

All laser tracks display enrichments in Cu and Ga from the cores to the borders of the metal grains investigated (Fig. 5) that define U-shaped zoning patterns. These profiles are sometimes asymmetric; the borders of the grains corresponding to the metal/matrix interfaces display lower Cu and Ga contents than the metal/chondrule interfaces (see profile 34-1A1 in Fig. 5). Maximum Cu contents range from 37 to 107 ppm and from 121 to 317 ppm for equatorial and nonequatorial sections, respectively (Table 3). The minimum Cu values measured in the cores of equatorial sections (8–14 ppm) are lower than in those of nonequatorial sections (24–75 ppm), as may be expected from sectioning artifacts. Maximum Ga contents range from 1.8 to 6.6 ppm in equatorial sections and from 3.7 to 8.9 ppm in nonequatorial sections (Table 3). Like Cu, the minimum Ga contents measured in the cores are lower in equatorial sections (0.5–0.9 ppm) than in nonequatorial sections (0.9–2.1 ppm).

The laser tracks passing through the center of two adjoining metal grains (2C1) display enrichments in Cu and Ga at the borders and at the interface between the grains (Fig. 5). The metal rims of 2C1 against the chondrules or matrix contain 45 and 36 ppm Cu, while the interface has the highest value of 78 ppm Cu. The EDS elemental map of S shows an enrichment of S along the interface leading to the possibility of beam overlap on the sulfide dominating this signature (Fig. 3b). The cores of the two metal grains contain <~10 ppm Cu. The chemical profiles measured for Ga are less well defined than for Cu, and also show that the rims and the interface are enriched in Ga relative to the cores of the metal grains Fig. 5).

Each diffusion profile is characterized by a diffusion length-scale (a), which can be expressed as:

$$a = 2\sqrt{D_X t} \qquad (1)$$

is characterized by a diffusion length-scale determined by numerically fitting an error function to the measured profiles of Cu using a MatLab routine.

D_X is the diffusion coefficient of the element X ($m^2\ s^{-1}$) and t the time (s). We numerically estimated the diffusion length-scale of each measured diffusion profile of Cu by fitting an error function. Values thus estimated range from 20 to 80 μm for Cu profiles measured through both equatorial and nonequatorial sections of metal grains, although the large metal grain enclosed within chondrule 1B has a diffusion length-

Table 1. Averaged compositions of the 22 tracks (15 µm spot size) measured in metal lumps associated with type I chondrules in Renazzo given in ppm (except for S, Fe, Co, and Ni, which are given in wt%).

	Equatorial sections									Nonequatorial sections												
	34-1A1	35-1A1	36-1A1	40-1A2	41-1A2	23-1B1	41-2C1	40-2C2	39-2C1/2	55-2A1	56-2A1	42-1F1	43-1F1	55-1E1	56-1E1	57-1E1	49-1E2	50-1E2	67-1C1	68-1C1	62-1C2	63-1C2
P	1734	1559	1853	1362	1470	2254	1600	1506	1422	3095	2466	3076	2581	2643	2870	2339	2729	2816	3176	3683	2994	3478
S	b.d.l.	b.d.l.	b.d.l.	b.d.l.	b.d.l.	b.d.l.	b.d.l.	b.d.l.	b.d.l.	b.d.l.	b.d.l.	b.d.l.	b.d.l.	b.d.l.	b.d.l.	b.d.l.	b.d.l.	b.d.l.	b.d.l.	b.d.l.	b.d.l.	b.d.l.
V	37	41	29	34	32	10	17	19	17	26	26	28	12	21	15	13	14	14	11	19	26	21
Cr	4313	4175	4217	4143	4380	1798	3347	3283	3234	3450	3225	3052	1852	2850	2363	2102	1990	2092	2640	2627	5966	5301
Fe	92.8	92.6	92.9	93.3	93.1	93.0	94.1	94.0	94.1	94.4	93.4	94.0	93.9	94.0	93.7	93.7	94.2	94.0	93.5	94.0	94.3	94.0
Co	0.313	0.315	0.296	0.299	0.297	0.320	0.319	0.309	0.326	0.247	0.233	0.263	0.277	0.267	0.275	0.278	0.262	0.247	0.259	0.285	0.238	0.249
Ni	6.31	6.48	6.17	5.85	6.05	6.26	6.42	6.49	6.51	5.03	4.64	5.16	5.38	5.21	5.44	5.59	5.03	5.24	5.65	5.05	4.58	4.89
Cu	36	43	26	28	21	17	14	24	18	104	108	80	69	34	44	48	78	76	130	118	116	154
Zn	n.a.	n.a.	n.a.	n.a.	n.a.	n.a.	2	3	b.d.l.	26	30	n.a.	n.a.	n.a.	n.a.	n.a.	n.a.	n.a.	n.a.	n.a.	n.a.	n.a.
Ga	3.2	2.8	2.0	2.5	1.8	0.8	1.1	1.6	1.1	2.0	3.8	3.9	3.6	2.0	1.7	1.6	2.0	2.1	1.9	4.3	3.5	3.2
Ge	b.d.l.	b.d.l.	b.d.l.	b.d.l.	b.d.l.	b.d.l.	b.d.l.	b.d.l.	b.d.l.	b.d.l.	b.d.l.	b.d.l.	b.d.l.	b.d.l.	b.d.l.	b.d.l.	b.d.l.	b.d.l.	b.d.l.	b.d.l.	b.d.l.	12.3
As	b.d.l.	3.3	b.d.l.	b.d.l.	b.d.l.	b.d.l.	b.d.l.	b.d.l.	b.d.l.	b.d.l.	b.d.l.	2.7	b.d.l.	1.9	b.d.l.	b.d.l.	2.8	b.d.l.	b.d.l.	2.6	b.d.l.	3.6
Mo	8.4	b.d.l.	b.d.l.	b.d.l.	b.d.l.	b.d.l.	16.6	21.1	16.7	27.4	16.3	b.d.l.	b.d.l.	b.d.l.	b.d.l.	b.d.l.	b.d.l.	b.d.l.	b.d.l.	11.6	b.d.l.	b.d.l.
Ru	2.1	2.5	1.9	2.6	2.3	3.1	3.8	3.8	3.8	2.0	2.0	2.0	2.1	2.1	2.2	2.0	1.9	2.4	0.7	0.9	0.8	0.9
Rh	0.36	0.34	0.33	0.35	0.39	0.50	0.77	0.67	0.73	0.48	0.51	0.32	0.34	0.34	0.35	0.32	0.36	0.43	0.14	0.14	0.22	0.22
Pd	2.1	2.2	2.2	2.3	2.0	2.4	2.1	2.4	2.0	2.2	2.0	2.0	2.3	1.9	2.5	2.2	2.0	2.3	2.4	2.6	2.3	2.8
Sn	n.a.	n.a.	n.a.	n.a.	n.a.	n.a.	0.1	b.d.l.	b.d.l.	b.d.l.	0.3	n.a.	n.a.	n.a.	n.a.	n.a.	n.a.	n.a.	n.a.	n.a.	n.a.	n.a.
Sb	n.a.	n.a.	n.a.	n.a.	n.a.	n.a.	b.d.l.	b.d.l.	b.d.l.	b.d.l.	b.d.l.	n.a.	n.a.	n.a.	n.a.	n.a.	n.a.	n.a.	n.a.	n.a.	n.a.	n.a.
W	0.21	0.32	0.21	0.24	b.d.l.	0.54	0.60	0.62	0.61	0.69	0.56	0.32	0.23	0.68	0.46	0.35	0.36	0.35	0.18	0.12	b.d.l.	0.17
Re	0.12	0.16	0.09	0.15	0.12	0.20	0.20	0.17	0.21	0.12	0.11	0.12	0.09	0.10	0.08	0.06	0.09	0.15	b.d.l.	0.04	0.03	b.d.l.
Os	1.07	0.91	1.07	1.57	1.73	1.82	2.41	2.11	2.23	1.60	1.49	0.93	1.02	1.01	1.22	1.11	1.04	1.12	0.08	0.05	0.21	0.42
Ir	1.05	0.84	0.91	1.51	1.51	1.81	2.05	1.99	2.09	1.28	1.21	0.91	0.94	0.92	1.02	0.89	1.01	1.22	0.12	0.08	0.20	0.34
Pt	2.39	1.85	2.01	2.38	2.59	3.57	4.84	4.59	4.59	2.35	2.19	2.10	2.22	2.09	1.89	2.23	2.46	2.30	0.27	0.18	0.30	0.74
Au	0.23	0.21	0.27	0.18	0.18	0.43	0.13	0.22	0.20	0.31	0.32	0.38	0.31	0.28	0.23	0.26	0.44	0.37	0.25	0.26	0.58	0.34

Average detection limits (in ppm, except for S, Fe, Co, and Ni which are given in wt%): P: 258; S: 0.8; V: 9; Cr: 88; Fe: 0.1; Co: 0.002; Ni: >0.01; Cu: 7; Zn: 3; Ga: 0.7; Ge: 7.7; As: 2.8; Mo: 7.4; Ru: 0.3; Rh: 0.15; Pd: 0.3; Sn: 0.2; Sb: 0.5; W: 0.07; Re: 0.02; Os: 0.02; Ir: 0.02; Pt: 0.04; Au: 0.04.

b.d.l. = below detection limit; n.a. = not analyzed.

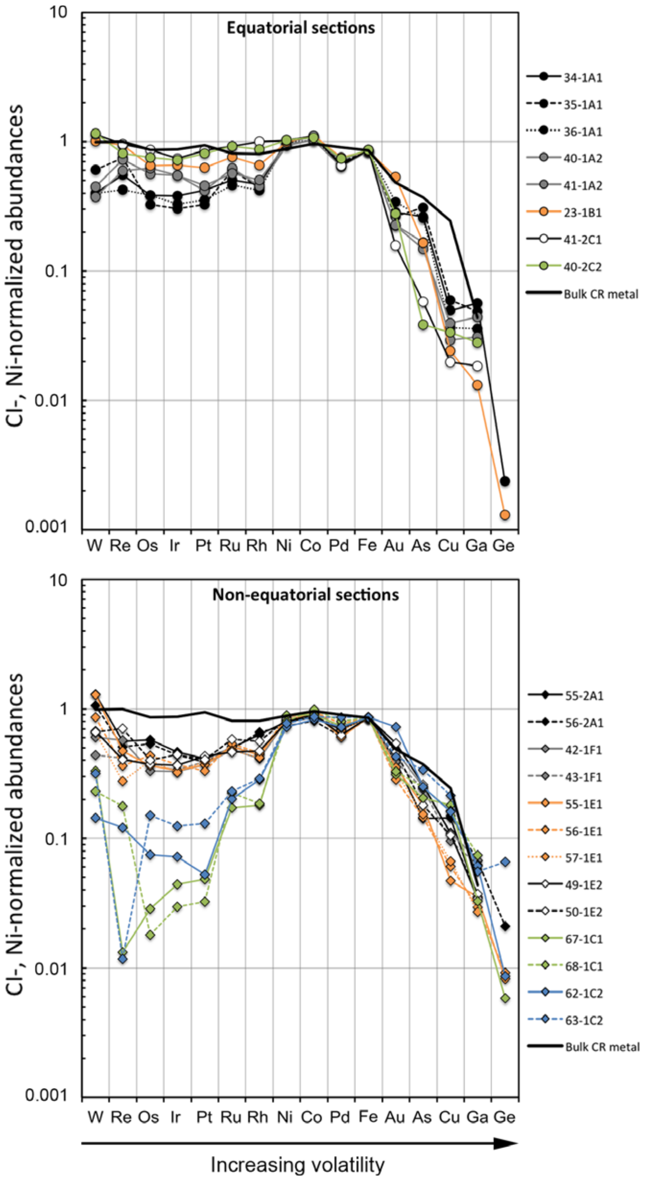

Fig. 4. Doubly normalized abundances (to CI chondrites and Ni) of siderophile elements for averaged track compositions obtained from equatorial and nonequatorial sections of metal grains shown as a function of volatility. The composition of bulk CR metal (Kong et al. 1999) is shown for comparison. In most of the analyses at the 15 µm spot size, the abundances of Ge and As are at or below the detection limits, while abundances of Ga and Cu are above the detection limits. (Color figure can be viewed at wileyonlinelibrary.com.)

scale of 260 µm (Table 3). The value of *a* for two elements of different diffusivities is different and can be given, for Cu and Ga, by:

$$\frac{a^2_{\mathrm{Cu}}}{D_{\mathrm{Cu}}} = \frac{a^2_{\mathrm{Ga}}}{D_{\mathrm{Ga}}} \qquad (2)$$

where a^2_{Cu} and a^2_{Ga} are the characteristic diffusion length-scales (m) of the Cu and Ga zoning profiles, respectively.

Peak Temperatures and Cooling Rates

Because all metal grains analyzed here display Cu and Ga zoning profiles, we used the method developed by Humayun (2012) to estimate the peak temperature (T_{p}) at which these profiles were formed and the associated cooling rates. The relative diffusivities of Cu and Ga have different activation energies (Righter et al. 2005), but there is a cross-over temperature at 1473–1523 K at which Cu and Ga have similar relative diffusivities. Cu diffuses slower than Ga at high temperatures, but faster at low temperatures. It is this temperature sensitivity of the Cu and Ga diffusivities that Humayun (2012) exploited to determine T_{p}.

Figure 6 shows the modeled correlation curves between Cu and Ga where their diffusion coefficients vary as a function of *T*, and Equation 2 is used to calculate a^2_{Ga} at a numerically calculated value of a^2_{Cu} over the temperature range of 1873–1273 K in 100 K increments. So, since Ga diffuses faster than Cu at 1873 K, a diffusion profile formed at this temperature will show a rapid increase in Ga at constant Cu followed by a gradual increase in Cu and plot along the uppermost curve in Fig. 6. At lower temperatures, e.g., 1273 K, that correspond to the lowermost curves in Fig. 6, the Cu content increases rapidly at nearly constant Ga values because Cu diffuses ~1 order of magnitude faster than Ga between 1173 and 1373 K. A modeled diffusion profile formed at 1573 K will plot along a straight line corresponding to the modeled Cu-Ga correlation at this temperature. The temperature of a diffusion profile is thus constrained by the correlation between Ga and Cu. For each profile measured, we can thus plot the data points on a Ga-Cu plot in which the modeled correlation curves are reported for different temperatures and using the values of a^2_{Cu} and a^2_{Ga} characteristic of the profile investigated. With the T_{p} values thus estimated, we can calculate the cooling rates associated using the relationship below:

$$\frac{\mathrm{d}T}{\mathrm{d}t} = \frac{-4D_{\mathrm{p}}RT^2_{\mathrm{p}}}{a^2\Delta H} \qquad (3)$$

where $\mathrm{d}T/\mathrm{d}t$ is the cooling rate (K s^{-1}), D_{p} the diffusion coefficient of Cu at peak temperature (m^2 s^{-1}), ΔH the enthalpy of activation for diffusion (J mol^{-1}), and *R* the gas constant (J m^{-1} K^{-1}). We used the enthalpy of activation and the diffusivities experimentally determined for Cu and Ga by Righter et al. (2005).

Table 2. Compositions of laser spots measured in the metal lumps associated with the chondrule 2C (see Fig. 3c for location) given in ppm (except for S, Fe, Co, and Ni, which are given in wt%).

Spot size (μm)	42-2C1 100	43-2C1 100	44-2C1 100	45-2C1 100	46-2C1 100	47-2C2 50	48-2C2 50	49-2C2 50	50-2C2 100	51-2C3 100
P	1617	1719	2020	1590	1747	1795	1675	2253	1751	1973
S	0.03	1.56	3.29	0.41	0.03	b.d.l.	b.d.l.	6.70	0.10	0.03
V	12	11	15	10	11	10	14	25	9	7
Cr	2722	2707	2553	2574	2806	2824	2959	4122	2996	3112
Fe	93.1	90.8	86.7	92.4	92.9	93.0	92.8	79.5	92.9	94.5
Co	0.310	0.322	0.312	0.313	0.312	0.306	0.314	0.353	0.310	0.253
Ni	6.05	6.05	5.86	6.12	6.21	6.10	6.36	5.58	6.11	4.59
Cu	11	77	152	36	13	20	13	308	28	20
Zn	0.5	32.0	108.8	15.9	0.5	1.6	1.3	208.3	2.2	0.4
Ga	0.7	2.7	5.3	1.3	0.7	1.1	0.9	10.9	0.9	0.7
Ge	0.4	6.8	15.4	2.5	0.4	0.7	**1.0**	45.3	1.6	0.3
As	0.9	1.6	1.4	1.0	1.0	1.1	0.9	2.6	1.0	1.3
Mo	6.7	6.2	5.9	6.5	6.8	9.0	7.4	5.5	7.0	5.2
Ru	4.7	4.4	4.4	4.7	5.0	4.8	4.7	4.4	4.9	4.3
Rh	0.82	0.78	0.74	0.80	0.82	0.84	0.82	0.83	0.80	0.68
Pd	2.5	2.4	2.3	2.5	2.4	2.4	2.5	2.5	2.4	1.9
Sn	0.04	0.12	0.34	0.07	0.04	0.05	0.05	0.61	0.03	0.04
Sb	0.07	0.06	0.11	0.06	0.04	0.04	0.04	0.22	0.03	0.03
W	0.65	0.65	0.63	0.65	0.68	0.71	0.71	0.83	0.71	0.48
Re	0.25	0.25	0.23	0.25	0.27	0.28	0.25	0.24	0.26	0.27
Os	2.83	2.92	2.69	2.93	3.14	3.22	3.00	2.88	3.27	3.99
Ir	2.81	2.77	2.61	2.79	3.03	2.96	2.81	2.74	2.99	3.60
Pt	5.56	5.36	4.98	5.36	5.84	5.73	5.56	5.41	5.58	5.14
Au	0.15	0.20	0.18	0.15	0.16	0.19	0.15	0.25	0.14	0.13

Average detection limits (in ppm, except for S, Fe, Co, and Ni, which are given in wt%) for the 100 μm spots: P: 7; S: 0.02; V: >1; Cr: 2; Fe: >0.1; Co: >0.001; Ni: >0.01; Cu: >1; Zn: 0.1; Ga: 0.2; Ge: 0.2; As: 0.1; Mo: 0.2; Ru: >0.1; Rh: >0.01; Pd: >0.1; Sn: >0.1; Sb: >0.1; W: >0.01; Re: >0.01; Os: >0.01; Ir: >0.01; Pt: >0.01; Au: >0.01; for the 50 μm spots: P: 17; S: 0.06; V: 1; Cr: 6; Fe: >0.1; Co: >0.001; Ni: >0.01; Cu: 1; Zn: 0.2; Ga: >0.1; Ge: 0.6; As: 0.2; Mo: 0.5; Ru: >0.1; Rh: 0.01; Pd: >0.1; Sn: >0.1; Sb: >0.1; W: 0.01; Re: >0.01; Os: >0.01; Ir: >0.01; Pt: >0.01; Au: >0.01.

b.d.l. = below detection limit.

These authors performed experiments at 1523–1673 K, 1 bar and 10 kbar, using diffusion couples composed of pure Fe and Fe-Ni alloys with 5.5% and 12.6% Ni containing 10–12 siderophile elements at natural abundance levels. Although the temperature range, Ni contents, and siderophile abundances during chondrule formation are similar to the experimental setting of Righter et al. (2005), the pressures investigated during these experiments are higher than what is expected in the chondrule-forming setting (~10^{-3} bar; e.g., Ebel and Grossman 2000). Experimental data from Righter et al. (2005), Goldstein et al. (1965), and Watson and Watson (2003) show that diffusivities increase when the pressure decreases, but the effect of pressure between 1 bar and 10^{-3} bar is negligible.

This relationship between T_p and cooling rate is based on the assumption that the resolution of the diffusion equation in the metal grains can be approximated by assuming a semi-infinite medium. The maximum values of Cu and Ga measured at the borders of the metal grains are lower than if they were formed by the equilibrium condensation from a gas of solar Cu/Ni and Ga/Ni ratios, 600 and 50 ppm for Cu and Ga, respectively. This implies incomplete condensation of Cu and Ga and other volatile elements and equilibrium with the gas that formed at the surface of the metal grain a rim with a constant composition. Although Cu and Ga diffused into the metal grain, the gas resupplied the rim so that it buffered the surface concentration. For this reason, a semi-infinite model is appropriate for solving the diffusion equation. With this framework, Cu and Ga diffuse from a half-space (the homogeneous rim enriched in Cu and Ga) with a concentration C_S, to another half-space (the interior part of the metal grain) with a concentration C_0. Thus, the solution of the diffusion equation has the form:

$$\frac{C(x,t) - C_s}{C_0 - C_s} = \mathrm{erf}(\frac{x}{2\sqrt{Dt}}) \tag{4}$$

where x is the distance (m) and $C(x,t)$ is the concentration of an element X at a given x and t.

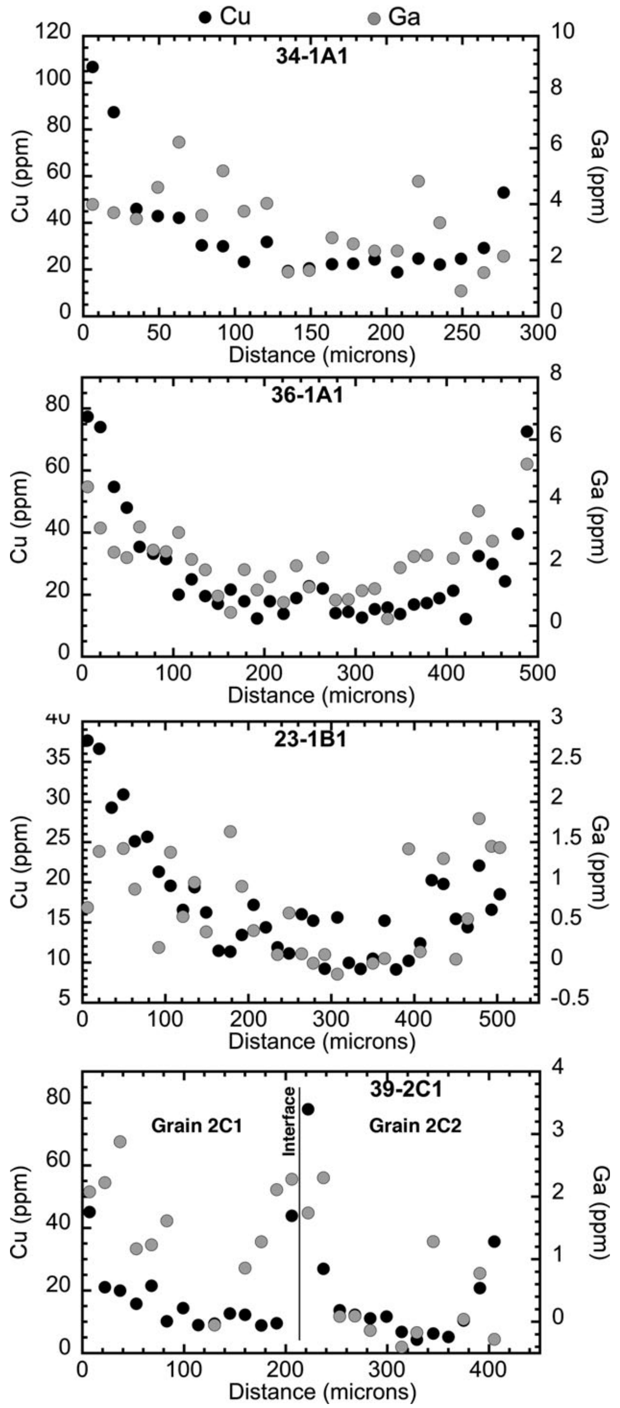

Fig. 5. U-shaped Cu (black dots) and Ga (gray dots) zoning profiles measured along the 34-1A1, 36-1A1, 23-1B1, and 39-2C1/2 laser tracks (see Figs. 2 and 3 for location). The profile 34-1A1 is asymmetric, the right side of the profile corresponding to the metal/matrix interface. The 39-2C1/2 laser track passes through the centers of the two adjoined metal grains 2C1 and 2C2 and shows a larger enrichment of Cu at the interface between them. Note the presence of sulfide along the interface in the BSE image (Fig. 3b) which likely contributes the additional Cu. Cooling rates were determined from the nonadjoining edges of these grains.

To investigate the reliability of our data, all the diffusion profiles measured for each grain were processed together. Thus, we called the "average" values of T_p and cooling rate the values calculated from all the diffusion profiles measured for each metal grain. The number of profiles analyzed, average values of the diffusion length-scales, and values of both T_p and cooling rates calculated in this work for each metal grain analyzed are reported in Table 3. The temperatures reported in Table 3 for each metal grain can be directly read in Fig. 6. The abundance of Ga measured in the cores of the metal grains is close to the detection limit (0.7 ppm). So, in Fig. 6, we did not plot the individual points situated in the center parts of the diffusion profiles. Instead we calculated an average for each core composition represented as squares in Fig. 6.

For equatorial sections, the mean values of the T_p calculated from the Cu-Ga plots (Fig. 6) range from 1623 to 1673 K (~1648 ± 55 K), with one exception. The latter corresponds to the laser track taken through the metal grain included within a type I chondrule (profile 23-1B1, Fig. 2b) which recorded a T_p of 1573 K. Excluding this grain, our results are ~175 K higher than the value obtained by Humayun (2012) for random sections (1473 ± 100 K). The mean values of cooling rates thus vary from 21 to 86 K h^{-1} for four of the five equatorial sections, while the cooling rate obtained for the profile 23-1B1 (1.2 K h^{-1}) is approximately an order of magnitude lower than values obtained from metal grains attached to the exteriors of type I chondrules. However, although this value of 1.2 K h^{-1} is significantly lower than the cooling rates calculated for the other equatorial sections, a single value is insufficient to generally conclude that cooling rates depend on the metal/silicate association. For four of the five equatorial sections, the maximum range of cooling rates is 6–241 K h^{-1} for T_p ~ 1503–1793 K (Table 3). For nonequatorial sections, the mean values of T_p range from 1473 to 1603 K (Fig. 6), slightly higher than the metal in the Acfer 097 CR2 chondrite (Humayun 2012) for reasons that are not obvious. For nonequatorial sections, the mean cooling rates range from 15 to 69 K h^{-1}. As could be expected for a group of metal grains cooling at different rates from a single gas, the equatorial sections show an inverse dependence of cooling rate with diffusion length-scale (Fig. 7).

Both T_p and cooling rates calculated here are roughly consistent from one metal grain to another for a single chondrule (Table 3). With the exception of the differences caused by the nonequatorial sectioning of some metal grains, the T_p and cooling rates are also roughly consistent from one type I chondrule to another. As discussed above, only one metal grain situated within chondrule 1B seems to have cooled

Table 3. Average diffusion length-scales (*a*), maximum and minimum contents measured for Cu and Ga, and T_P and associated cooling rates (mean value and maximum possible range) calculated for each metal grain analyzed.

					Cu (ppm)		Ga (ppm)		T_p (K)		dT/dt (K h^{-1})	
	Chondrule	Grain #	*n*	*a* (mm)	Max.	Min.	Max.	Min.	Mean	Max. possible range	Mean	Max. possible range
Equatorial sections	1A	1A1	3	80	107	13	6.6	0.8	1623	1503–1743	21	6–62
		1A2	2	75	77	14	5.4	0.5	1653	1553–1753	32	12–77
	1B	1B1	1	260	37	9	1.8	0.8	1573	1503–1643	1.2	0.6–2.4
	2C	2C1	2	50	45	8	2.8	0.7	1673	1553–1793	86	27–241
		2C2	2	70	72	10	3.7	0.9	1653	1573–1733	37	17–75
Nonequatorial sections	2A	2A1	2	45	317	51	4.9	1.6	1523	1353–1693	24	3–128
	1C	1C1	2	20	274	71	5.7	1.8	1473	1353–1593	69	15–251
		1C2	2	35	220	75	8.9	1.2	1503	1353–1653	32	5–146
	1E	1E1	3	85	121	24	3.7	1.1	1603	1453–1753	15	3–60
		1E2	2	35	242	43	4.3	0.9	1473	1373–1573	22	6–67
	1F	1F1	2	65	149	41	7.2	2.1	1603	1473–1733	25	7–80

n = number of profile measured for each grain.

significantly slower than the other metal grains. The difference observed might be attributed to the insulating effect of the surrounding silicates. During cooling, the heat loss rate of the metal grain would have been lower than those of the metal grains attached to the exteriors of type I chondrules and (partially) exposed to the surrounding gas.

The relation between cooling rates and T_p for the equatorial sections of metal grains is illustrated in Fig. 8, which highlights that the higher cooling rates correspond to the higher T_p.

DISCUSSION

Bias and Uncertainties: Natural and Analytical Origins

A geometrical bias is introduced for the zoning profiles of nonequatorially sectioned metal grains. For a spherical metal grain, the center of a chemical zoning profile that does not pass through the actual core of the grain will display a higher Cu (and Ga) concentration (C_0) than the center of a chemical profile passing through the actual core of the grain. Because the surface concentration (C_S) is similar on both nonequatorial and equatorial profiles, this difference of C_0 will imply a gentler gradient for the nonequatorial profile, which yields a lower cooling rate. For example, at a constant value of T_p of 1623 K, the cooling rates calculated for diffusion length-scales of 80 and 100 μm are 21 and 13 K h^{-1}, respectively. Figure 7 compares the cooling rates as a function of the diffusive length-scale for both equatorially and nonequatorially sectioned metal grains from Renazzo. Although cooling rates calculated from equatorial sections seem to be higher than those from nonequatorial sections, they are not distinguishable for diffusion length-scales higher than 70 μm (Fig. 7). This study yielded sufficient data for equatorially sectioned grains to test models of chondrule formation.

At Cu and Ga abundances near the edges of metal grains in Renazzo, the analytical uncertainties are better than 5%. These analytical uncertainties are small compared to the variations of the calculated cooling rates caused by the sectioning of the metal grains. To estimate the reliability of the calculated cooling rates, we analyzed multiple metal grains and measured several diffusion profiles on each grain. Because of this approach, the ranges of T_p and cooling rates reported in Table 3 are mostly due to natural variability.

As illustrated by the 34-1A1 profile in Fig. 5, the zoning profiles analyzed are asymmetrical when the metal grains investigated are in contact with the surrounding matrix, with the metal adjacent to the matrix having lower Cu and Ga contents than when adjacent to the chondrule side. This geometric feature can be due to the irregular shapes (nonspherical) of the metal grains investigated. Moreover, petrologic observations of the metal grains in Renazzo indicate that parent body alteration also needs to be considered as a source of such asymmetric zoning profiles (Fig. 2a). For example, the termination of grain 1A1 against the matrix appears to have lost most of its zoning in Cu and Ga, and the border with the matrix appears to be corroded (Fig. 2a).

Numerous CR chondrites, and in particular Renazzo, have undergone parent body aqueous alteration (e.g., Harju et al. 2014; Schrader et al. 2014; Le Guillou et al. 2015). Although goethite is commonly described as a terrestrial weathering product (e.g., Rubin 1997; Wasson and Rubin 2009), iron oxide and sulfide layers around metal grains in highly altered CR chondrites (e.g., Renazzo, Al Rais) were likely formed during parent body alteration (e.g., Morlok and

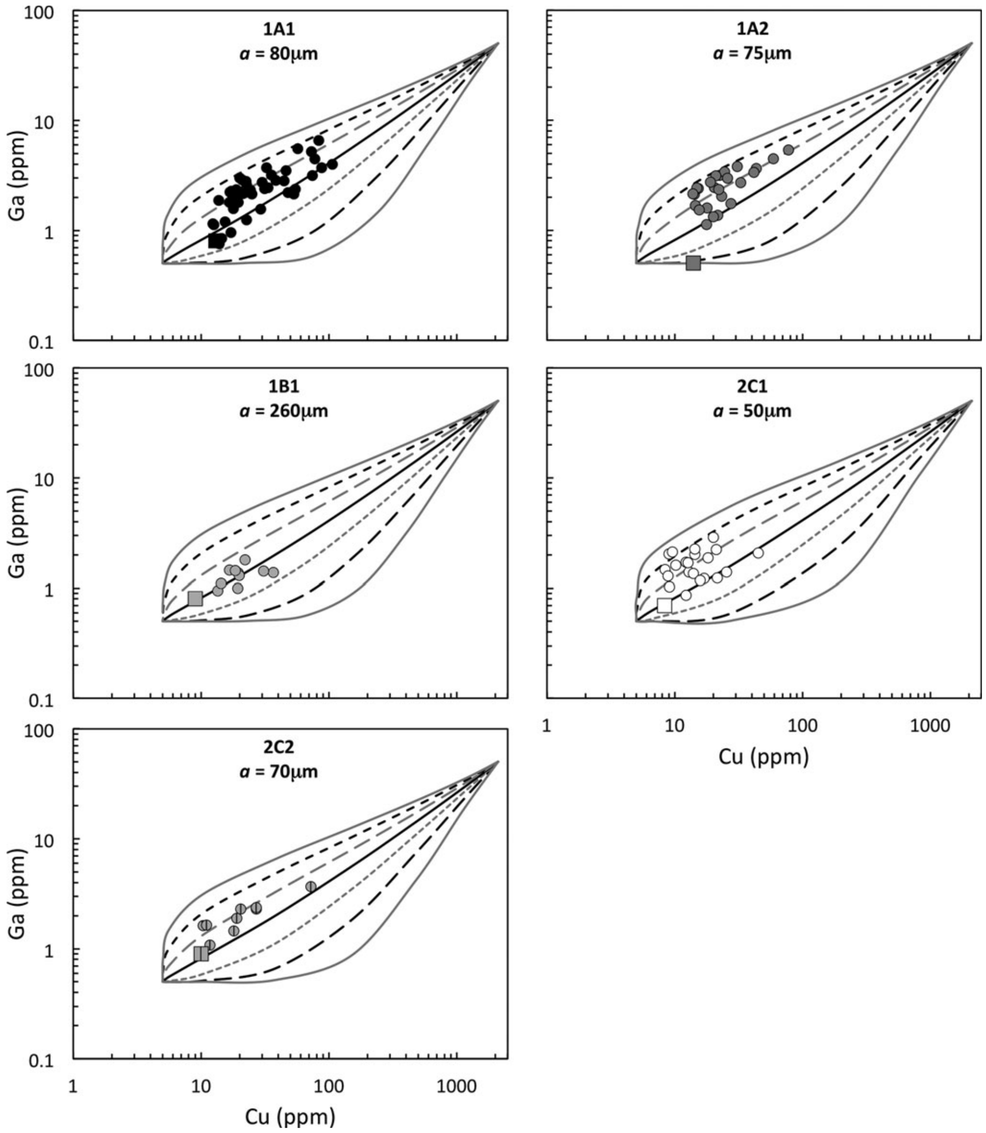

Fig. 6. Ga versus Cu plots for equatorial and nonequatorial sections of metal grains, for the 11 metal grains measured either included within (1B1), or attached to the surfaces (all other metal grains) of seven chondrules in Renazzo. Using the average value of the diffusion length-scales (a_{Cu}) calculated for each metal grain, we drew for comparison the diffusive trajectories of Ga versus Cu as a function of temperature from 1873 K (uppermost curve) to 1273 K (lowest curve) in 100 K increments. Since Ga contents in the cores of metal grains are close to the detection limit (~0.7 ppm), we did not plot the individual points situated in the center parts of the diffusion profiles, but calculated an average for each core composition. The average Cu and Ga core compositions of each metal grain investigated are plotted using colored squares.

Libourel 2013; Harju et al. 2014). Fe-Ni metal is partially replaced by magnetite and sulfide during the dissolution and transport of S from the matrix to form alteration rinds around metal. Metal grains are thus more altered at their matrix/chondrule boundaries, as indicated by the lobed texture situated on the matrix side of several metal grains analyzed (Fig. 2a). As a consequence of the destabilization of primary Fe-Ni metal into iron oxides and sulfides during parent body alteration, the original grain boundaries of the metal grains that contained the highest Cu and Ga contents cannot be analyzed anymore. The ranges of Cu and Ga contents measured for such grains are thus lower than before parent body alteration. Nevertheless, as discussed by Humayun (2012), this process cannot completely erase or modify the original Cu and Ga zoning profiles. Although the highest Cu and Ga contents are lacking on the Ga-Cu plots, the remaining part of the data still defines the same trend. The modeled Cu-Ga correlation lines defining the values of T_p can be slightly different due to the smaller diffusion length-scale after grain-boundary alteration (see the Peak Temperatures and

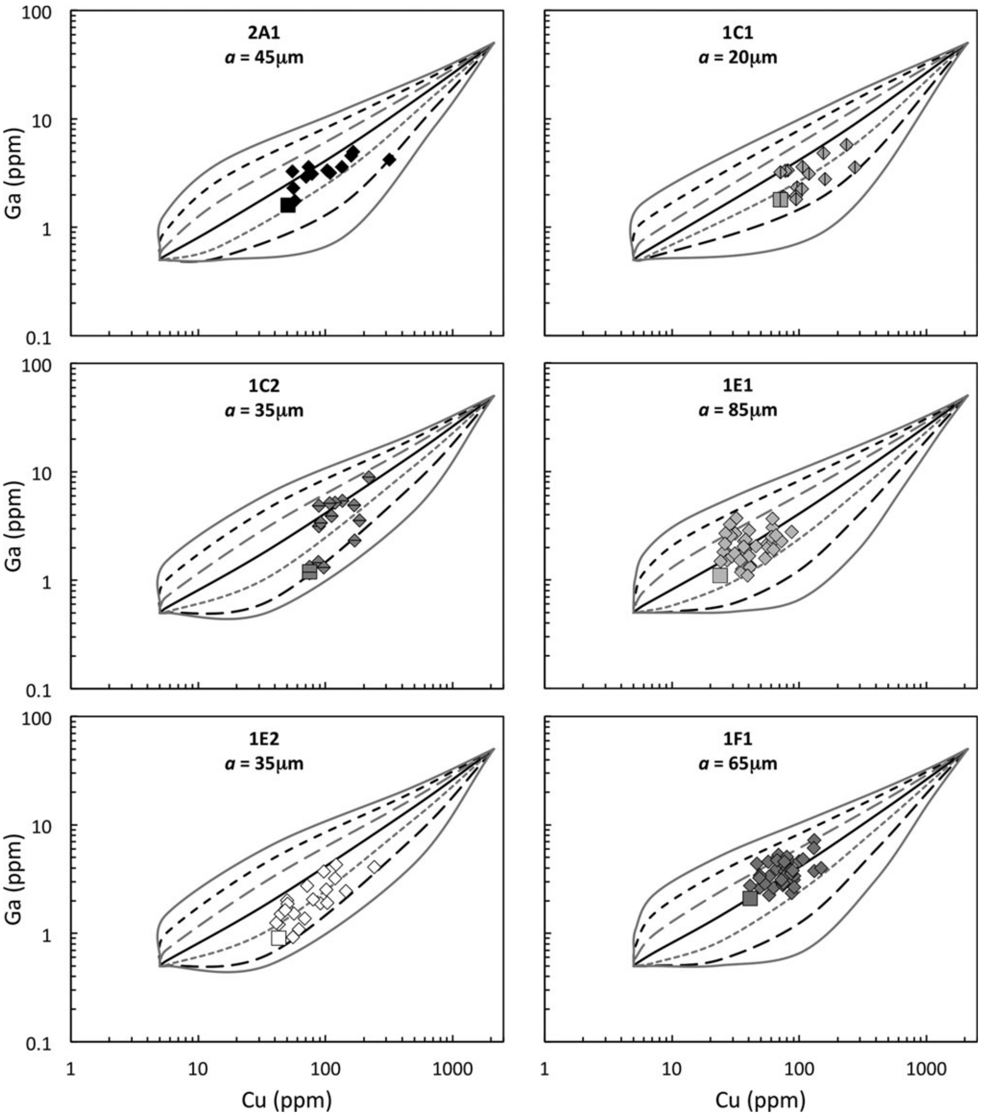

Fig. 6. Continued.

Cooling Rates section). However, these differences are not significant, in particular for the range of T_p calculated in this work (~1600–1700 K).

Origin and Formation of Cu and Ga Profiles

Measurements of trace siderophile and major element abundances in metal from CR chondrites (Kong and Palme 1999; Kong et al. 1999; Humayun et al. 2002, 2010; Zanda et al. 2002) indicate that metal was partially depleted in volatile elements such as Cu, Ga, Ge, and Au by evaporation during melting events that formed Renazzo chondrules. Moreover, the metal grains that rim chondrules in CR chondrites are considered to have formed from a liquid (Wasson and Rubin 2010). Below the melting point of Fe-Ni alloy (~1800 K), volatile siderophile elements thus recondensed at the surface of the metal grains (Kong et al. 1999; Connolly et al. 2001; Hewins and Zanda 2012; Humayun 2012). As a consequence, solid metal grains were enriched in volatile elements on their exteriors, and these volatile elements diffused inward during cooling. Because Cu and Ga zonation profiles can only survive if the metal is solid, this progressive enrichment of the metal in volatile elements during cooling caused by the progressive recondensation of Cu (and other volatile elements) must have occurred between 1800 K and the condensation temperature of Cu, i.e., 1200 K (Humayun 2012).

Our measurements display Cu and Ga enrichments all around the metal grains, even those situated in chondrule interiors, and at the interfaces between distinct grains. This ubiquity of U-shaped profiles possibly indicates that large metal grains located

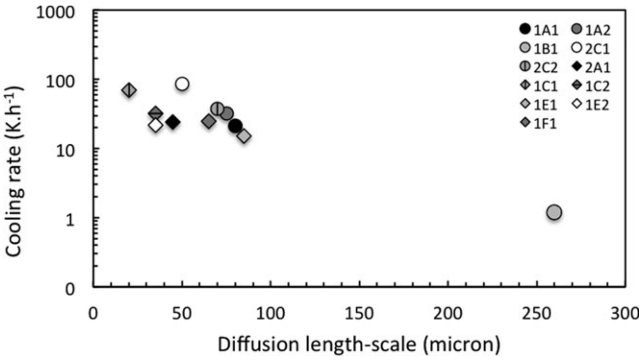

Fig. 7. Cooling rates (mean values) plotted as a function of the mean diffusion length-scale for Cu zoning profiles for both equatorial (circles) and nonequatorial (diamonds) sections.

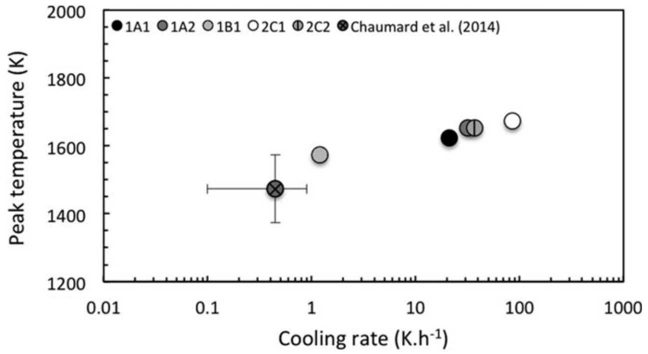

Fig. 8. Mean peak temperatures (T_p) versus mean cooling rates calculated from Cu zoning profiles through equatorial sections of metal grains in Renazzo. Also shown is the cooling rate inferred from a millimeter-sized metal grain isolated in the matrix of Renazzo (red circle) measured through its equatorial section using the same Cu-Ga method (Chaumard et al. 2014).

alongside and within type I chondrules reacted with the ambient gas (evaporation and recondensation of volatile siderophile elements) before being aggregated and/or incorporated into the chondrules. Based on the constraint that metal lumps were initially liquid to allow evaporation of volatile siderophile elements, zoning profiles measured here suggest that, at least, large metal grains solidified and then reacted with the gas before being associated with the chondrule silicates. During incorporation of the solid metal grains, silicate melt and crystals are both present. Using the MELTS program (e.g., Ghiorso and Sack 1995; Asimow and Ghiorso 1998), the crystallization of a silicate melt with the bulk composition of a type IAB chondrule (POP chondrule C50 analyzed by Jones [1994] in Semarkona) starts at approximately 1830 K with the formation of olivine (~$Fo_{97.3}$). Diopside starts to crystallize at ~1410 K, so that a silicate melt is still present during the formation of the Cu and Ga zoning profiles in solid metal grains (1575–1675 K for equatorial sections of metal grains), down to the glass transition temperature.

The narrow range of Cu and Ga contents measured in the core of the equatorial sections of metal grains (8–19 and 0.5–1.6 ppm, respectively) indicates that they have probably all been thermally processed to the same extent. Because the size of the metal grains analyzed is highly variable (from ~190 to 500 μm for equatorial sections), the initial Cu and Ga contents in the former liquid metal before solidification would have been roughly similar from one droplet to another. In consequence, metal droplets must have evolved either within the same gas or within different reservoirs with comparable Cu and Ga partial pressures.

Where Did The Liquid Metal Come From?

It has been recognized that liquid metal and liquid silicate cannot form as condensates from a nebular gas with a solar composition in a minimum mass nebula because these liquids are not stable under 10^{-3} to 10^{-6} bar (e.g., Yoneda and Grossman 1995; Ebel and Grossman 2000; Ebel [2006] and references therein). To keep a liquid metal droplet as a stable condensate relative to the surrounding gas at temperatures higher than ~1800 K (melting point of Fe-Ni alloy), dust enrichments up to ×1000 relative to CI chondrites and thus high partial pressures of Fe are required (e.g., Ebel and Grossman 2000). It has been found that unzoned metal grains in CB chondrites formed by an equilibrium condensation process at P^{tot} of 10^{-2} bar and a Ni/H enrichment of 3×10^3 relative to the solar composition (or P^{tot} of 10^{-3} bar and a Ni/H enrichment of 3×10^4), conditions at which the equilibration temperatures of these metal grains imply that they condensed from a vapor as liquids (Fedkin et al. 2015). These conditions, at odds with canonical solar nebula conditions (Fedkin and Grossman 2013; Fedkin et al. 2015), are consistent with condensation of liquid metal in a vaporized impact plume at high temperatures (>1900 K), as suggested previously (Campbell et al. 2002; Krot et al. 2005; Oulton et al. 2016). Despite mineralogical, petrographic, and isotopic similarities of the chondritic components from the CB and CR chondrites (e.g., Weisberg et al. 1993; Krot et al. 2002), the CR metal studied here lacks the chemical characteristics of CB metal, like high Pd/Ir ratios, that clearly identify CB metal as a condensate from a high-pressure impact vapor plume (Campbell et al. 2002; Fedkin et al. 2015).

The nearly chondritic patterns of refractory siderophile elements measured in this work for some metal grains might support the idea that metal was formed by condensation as a liquid. The subchondritic refractory element abundances measured in numerous metal grains are best explained by the addition of Fe-Co-Ni by recondensation to the surface of these original precursors thus diluting the refractory elements (Fig. 4). Although some of our chemical results can be consistent with an origin of metal droplets by condensation from a dust-rich gas under high total pressures, the laser spot 51-2C3 (Fig. 3c) displays Re, Os, and Ir enrichments characteristic of formation by fractional crystallization from a liquid metal. The first solid metal that crystallizes from a liquid metal is enriched in compatible refractory elements such as Re, Os, and Ir relative to the residual liquid metal. Thus, the role of an igneous process, i.e., solid metal–liquid metal fractionation, is evident in this grain (grain 2C3; Fig. 3a).

The depletion of chondrules in siderophile elements relative to CI chondrites (e.g., Sears et al. 1996) was interpreted as a record of metal being formed in chondrules and expelled from the chondrule melt when it was still liquid (e.g., Connolly et al. 2001). Recently, Chaumard et al. (2014) proposed an igneous origin for a millimeter-sized metal grain isolated in the matrix of Renazzo. The expulsion of metal droplets from chondrule melts was theoretically investigated by Uesugi et al. (2008) who studied the kinetic stability and the conditions required for the ejection of a melted iron globule from the inside of a melted chondrule. These authors showed that surface tension forces were sufficient to eject most of the metal globules present within melted chondrules even without angular momentum (nonrotating model). Wasson and Rubin (2010) proposed a variant of this model to explain the Fe-Co-Ni systematics of CR metal. So, considering that metal in CR chondrites originated from chondrules (e.g., Connolly et al. 2001; Zanda et al. 2002), our data imply that large metal grains were isolated previously from the liquid silicate as immiscible liquids, then cooled, crystallized, and re-accreted within partially molten chondrules (see the Origin and Formation of Cu and Ga Profiles section) after reacting with the surrounding gas. Whether liquid metal drops were expelled from chondrule melts or condensed from a gas, the ubiquity of Cu zoning profiles supports formation of chondrules in Renazzo by aggregation and coalescence of droplets, as advocated by Zanda et al. (2002). Within this framework, the presence of metal blebs within chondrules is understood as the engulfing of metal droplets from a spray, within silicate droplets in an expanding impact plume (Asphaug et al. 2011; Sanders and Scott 2012). If such a metal spray originates from the core of a differentiated planetesimal, fractional crystallization patterns inherited from the metal precursor may be expected in the chondrule metal. The presence of ubiquitous depletions observed for compatible elements and the comparative lack of corresponding excesses in compatible elements (Fig. 4) (with the notable exception of 51-2C3, Fig. 3) are consistent with an impact spray model for CR metal.

Wasson and Rubin (2010) argued that the uniform distribution of metal on chondrule surfaces can be interpreted as the result of the segregation of a liquid metal through channels in the silicate melt or at interfaces between silicate crystals. This mechanical process of metal liquid droplets that migrate to the surfaces of chondrules would have been governed by the surface and interfacial tensions, as advocated by Wood (1963) and Uesugi et al. (2008), although other studies preferred centrifugal forces (e.g., Grossman and Wasson 1985; Kong and Palme 1999; Humayun et al. 2002). This mechanism implies that metal droplets crystallized at the surface of chondrules or in chondrule interiors, but not within the gas. Only surfaces of metal grains exposed to the gas would have been enriched by the recondensation of Cu and Ga that diffused inward. An alternative origin of the Cu and Ga zoning profiles observed at surfaces in contact with the silicate portion of the chondrules may thus be invoked. As discussed in the Origin and Formation of Cu and Ga Profiles section, the complete crystallization of a silicate melt with a type IAB bulk composition is not achieved when the Cu and Ga zoning profiles formed in the solid metal grains. It is thus conceivable that the zoning profiles may come from the interactions between the solid metal and the melt of the partially molten chondrule. This scenario would assume that Cu and Ga recondensed on the surface of a partially molten chondrule, so that the rate-limiting diffusion process occurred in the solid metal in which the zoning profiles are preserved. Additional data such as the distribution of Cu and Ga in chondrule silicates and in the mesostasis are required to investigate this scenario.

Comparison with Other Estimates of Cooling Rates

In Situ Measurements of Cooling Rates

Only a few measurements of cooling rates have been made on type I chondrules so far. Cu and Ga zoning profiles measured on metal grains attached to type I chondrules from the Acfer 097 CR2 chondrite have been used by Humayun (2012) to calculate cooling rates. The latter reported values ranging from 0.5 to 50 K h^{-1} for $T_p \sim 1473 \pm 100$ K, with a maximal possible range of 0.1–400 K h^{-1} for $T_p \sim 1200$–1800 K. The cooling rates and to a lesser extent the T_p values calculated in this work (1.2–86 K h^{-1} for $T_p \sim 1573$–1673 K) are in good agreement with the results of Humayun (2012). In addition to being consistent from one chondrule to another (see the Comparison With Other Estimates of Cooling Rates section), these similarities of cooling rates and T_p for the two CR2 chondrites, Renazzo and Acfer 097, indicate that the range of thermal histories of type I chondrules is also likely consistent from one CR chondrite to another.

This conclusion supports a common origin of type I chondrules from CR chondrites, as may be expected. The range of cooling rates obtained for the seven chondrules analyzed here thus strengthen the idea that all type I chondrules in CR chondrites may have shared a common thermal history.

Cooling rates calculated from Cu zoning profiles in metal grains are also in good agreement with those obtained from pyroxene exsolution in type I chondrules. Weinbruch and Müller (1995) reported cooling rates of 2–10 K h^{-1} for $T_p \sim 1473$–1623 K for type I chondrules in the CV3 Allende. For a type IAB porphyritic chondrule in the Paris CM chondrite, Cuvillier et al. (2014) calculated cooling rates ranging from 10 to 100 K h^{-1} for $T_p \sim 1473$ K. These measurements of cooling rates of type I chondrules in various groups of CCs using different methods imply that type I porphyritic chondrules in CCs may have been formed during one or more similar high-temperature event(s).

Cooling Rates Inferred From Experimental Studies

Most of the thermal constraints on chondrule formation and cooling rates are provided either by the experimental investigation of chondrule textures or chemical zoning profiles of single olivine crystals from type II chondrules. Based on mineral textures, two sets of experiments on type I porphyritic chondrules reported cooling rates in the range of 10–1000 K h^{-1} (Radomsky and Hewins 1990; DeHart and Lofgren 1996). Wick and Jones (2012) found that analogs of plagioclase-bearing type I chondrules from CO chondrites could be produced if the cooling rate was reduced to 1 K h^{-1} near the solidus (1273–1073 K). Type I chondrules in CR chondrites contain plagioclase (e.g., Jones 2014; Tenner et al. 2015), but often as an accessory phase. The scarcity of plagioclase-bearing chondrules in CR chondrites implies higher cooling rates for CR chondrules. The lowest values of the cooling rates experimentally estimated from chondrule textures are consistent with the range of cooling rates obtained in this study (1.2–86 K h^{-1}) but extend to much higher cooling rates. However, these experimentally determined cooling rates in silicates are not in conflict with the cooling rates estimated from Cu-Ga zoning profiles in metal grains. Indeed, they correspond to processes that occurred at higher temperatures (above the type I chondrule solidus) than the formation of the Cu and Ga diffusion profiles measured here.

Recently, Villeneuve et al. (2015) proposed that type II chondrules mainly derived from the reheating of type I precursor materials at 1723–1773 K under oxidizing conditions (between the IW and NNO buffers), and concluded that the formation of olivine-rich chondrules was a fast process. After an initial slow cooling episode at high temperature (1773–2073 K) during a short time scale (< few hundreds of minutes), they required rapid cooling rates ($>10^3$–10^4 K h^{-1}) for olivine-rich chondrules. The cooling history proposed by Villeneuve et al. (2015) appears to be inconsistent with our cooling rate results (Fig. 9).

Chondrule Formation Models

The cooling rates determined above place constraints on the various chondrule formation models proposed so far. The characteristic cooling rates of nebular lightning models should likely be on the order of several thousand K h^{-1} depending on the gas density and discharges of electrical energy (e.g., Desch and Cuzzi 2000). The cooling rates calculated for equatorial sections (1.2–86 K h^{-1}) and values estimated from experiments on type I porphyritic chondrules are clearly inconsistent with the fast cooling rates predicted by the lightning model (Morfill et al. 1993; Pilipp et al. 1998; Desch and Cuzzi 2000) (Fig. 9).

Unlike the lightning model, the X-wind model (e.g., Shu et al. 1996, 2001) predicts some of the lowest cooling rates (~6–10 K h^{-1}; Desch et al. 2010, 2012). These cooling rates are only consistent with the lowest values experimentally estimated for the formation of the porphyritic textures of chondrules and are lower than the values measured in this work for equatorial sections (21–88 K h^{-1}) (Fig. 9). Moreover, cooling rates predicted by the X-wind model are nearly constant during time, from the peak temperature, implying linear cooling curves (Fig. 9). The cooling rate of a chondrule in the X-wind model depends on how fast it can move away from the Sun since thermal radiation from the Sun controls the cooling rate, not gas opacity. As noticed by Desch et al. (2012), since the blackbody temperature of an object varies with the heliocentric distance, the cooling rate of a chondrule is only a function of the peak temperature, heliocentric distance, and radial velocity, hence it experiences a constant cooling rate in the X-wind. The faster cooling rates systematically associated with the highest T_p for chondrules in Renazzo (Fig. 8) are not consistent with the cooling curve predicted by the X-wind model.

Recently, Fedkin and Grossman (2013) performed equilibrium calculations to investigate the vapor saturation of the gas and the chemical and mineralogical evolution of droplets formed under conditions satisfying Na retention. The authors found that chondrules were formed in dust-enriched environments under high total pressures. These results were interpreted to be consistent with a formation in impact-generated plumes rather than in a nebular setting. Based on studies of Na retention during

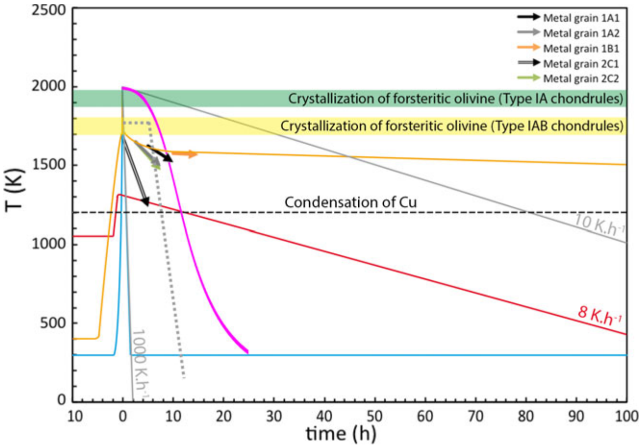

Fig. 9. Temperature–time evolution for type I chondrules determined using the equatorial sections of the metal grains analyzed (arrows) compared with other empirical cooling rate constraints and with predictions from chondrule formation models. Predicted thermal histories from the X-wind model (adapted from Shu et al. 1996) (red curve), lightning models (e.g., Desch and Cuzzi 2000) (blue curve), impact jetting (Johnson et al. 2015) (purple curve), and shock wave models (adapted from Morris and Desch 2010) (orange curve) are shown. Each arrow starts at the mean temperature calculated for each grain and the slope corresponds to the dT/dt associated. Arrows are reported along the x-axis and tied to the point at which the shock wave curve passes through the T_p of the metal grains. The shock wave curve shown can be related to the "case 17" reported by Morris and Desch (2010) ($C = 50$, $V_S = 8$ km s^{-1}, $\rho_g = 10$ g cm^{-3}). The range of temperatures experimentally determined for the crystallization of forsteritic olivine in type IA (green area) and IAB (yellow area) chondrules (see text for references) and the condensation temperature of Cu in a gas of solar composition at pressure sufficient to condense liquid iron (dashed black line) are shown. The gray lines correspond to the minimum (10 K h^{-1}) and maximum (1000 K h^{-1}) values of cooling rates inferred from crystallization experiments (see text for references), and the gray dotted curve to the schematic thermal evolution proposed by Villeneuve et al. (2015) from heating experiments of type I chondrules.

chondrule formation and the high dust/gas ratio necessary to explain the volatile contents measured in chondrules (Alexander et al. 2008; Alexander and Ebel 2012; Fedkin and Grossman 2013), Johnson et al. (2015) developed a numerical model to investigate the possible production of chondrules during impacts between planetesimals. Compared to the splashing model in which droplets from the liquid interiors of planetesimals are launched into a plume by impact (Asphaug et al. 2011; Sanders and Scott 2012), jetting implies the melting of solid material by kinetic energy during hypervelocity impacts (Johnson et al. 2015). In the jetting model, the presence of possible metal-sulfide liquids in association with silicate droplets is not specifically discussed (Johnson et al. 2015). However, impact jetting simulations reproduce numerous chondrule features such as their sizes, and predict that jetted material cools nonlinearly at rates ranging from 10 to 1000 K h^{-1}. These cooling rates are consistent with the results from experimental studies on chondrule textures. We note here that the highest values correspond to the outermost part of the plume, which radiates into the interplanetary medium, taken as 300 K in the numerical simulations of Johnson et al. (2015). During expansion, the thermal evolution of the material of such a plume is characterized by an increase in the cooling rates between 2000 and ~1500 K (from 10 to ~150 K h^{-1}), then a decrease to a few K h^{-1} (e.g., ~20 K.h^{-1} at 400 K) between ~1500 K and the thermal re-equilibration of the plume with the interplanetary medium (Johnson et al. 2015). This initial increase in cooling rate from 2000 to ~1500 K would define a negative correlation in a T_p versus cooling rate plot. The relationship between the peak temperatures and cooling rates calculated for type I chondrules in Renazzo is not in agreement with these numerical results (Fig. 9). The higher cooling rates systematically correspond to higher temperatures (see the Comparison With Other Estimates of Cooling Rates section and Fig. 8), in the range of ~1500–1800 K.

The best-developed models for chondrule formation invoke nebular shock waves passing through the protoplanetary disk (e.g., Wood 1963; Hood and Horanyi 1991; Ciesla and Hood 2002; Desch and Connolly 2002; Morris and Desch 2010). However, some caveats have been pointed out about the viability of shock models for chondrule formation. In the case of an optically thick disk, using the input parameters of Desch and Connolly (2002), shock waves with velocities relative to the gas lower than 6.5 km s^{-1} are unable to completely melt the chondrule precursors and also produce cooling rates dropping to zero at ~1600 K (Stammler and Dullemond 2014). However, T_p, which is strongly a function of the gas density, can nevertheless reach values high enough for the melting of chondrule precursors for shock speeds >7.0 km s^{-1} (Desch and Connolly 2002; Morris and Desch 2010). For an optically thin disk, where the precursors can freely lose their energy by radiation, the shock velocities need to be higher than 9.0 km s^{-1} for melting. In this case, the cooling rates for $T_p > 1500$ K are too high to be consistent with the chondrule textures (1 and 2×10^5 K h^{-1} for T_p ~1550 and 1750 K, respectively; Stammler and Dullemond 2014). Moreover, numerical modeling of destructive collisions in nebular shocks predict that shock wave models for chondrule formation are inconsistent with high solid/gas ratios relative to the solar value because of the sandblasting effect caused by the finest particles (Jacquet and Thompson 2014). In addition to the fact that high solid/gas ratios are required for Na retention (see above), these results suggest that large-scale shock waves appear inefficient for chondrule formation.

The two leading models proposed for the source of shock are gravitational instabilities and bow shocks around planetesimals. These models have been reasonably successful at predicting cooling rates required to produce chondrule textures (e.g., Desch and Connolly 2002; Morris et al. 2012). In addition to reproducing the cooling rates of ~10–1000 K h^{-1} experimentally estimated for chondrules (e.g., Lofgren 1996; Hewins et al. 2005; Wick and Jones 2012), the shock wave models predicted a nonlinear cooling curve characterized by a decrease of the cooling rate with time (Fig. 9). After the shock passes, a peak temperature of around 2000 K is reached in the gas. From this peak temperature, cooling rates below the liquidus temperature of chondrules are predicted to be initially high (~10^3–10^4 K h^{-1}), which is in contradiction with the Na saturation in the vapor reached within seconds when chondrules start to cool at ~10–100 K h^{-1} at near-liquidus temperatures (Fedkin et al. 2012). During the crystallization of olivine (from 1700 to 1900 K to ~1500 K; e.g., Miyamoto et al. 2009), the cooling rates of chondrules inferred from the shock models drop to values ranging from ~10 to several hundreds K h^{-1} depending on the abundance of chondrules within the gas (Morris and Desch 2010). These predictions are fully consistent with our results (21–86 K h^{-1} for T_p of 1623–1673 K), as well as the lowest cooling rates experimentally determined (e.g., Radomsky and Hewins 1990; DeHart and Lofgren 1996; Lofgren 1996; Hewins et al. 2005; Wick and Jones 2012). Although the faster cooling rates calculated in this work are associated with the highest T_p, we cannot conclude at this point that the cooling of type I chondrules was nonlinear. Indeed, only one element pair (Cu-Ga) was used for the different chondrules analyzed. Measuring cooling rates at various T_p recorded by different element pairs would provide better evidence for such thermal evolution during chondrule formation.

CONCLUSION

All metal grains investigated in Renazzo preserved chemical zonation for Cu and Ga. These diffusive zoning profiles, which are the result of the recondensation of the volatile elements during cooling, were used to characterize the solid-state thermal history of chondrules. Using computed X-ray tomography, equatorial sections of metal grains were obtained that avoid underestimation of cooling rates and peak temperatures due to nonequatorial sectioning. With the exception of a metal grain embedded in the core of a chondrule that exhibits a cooling rate of 1.2 K h^{-1} for T_p ~ 1573 K, the cooling rates thus estimated for type IAB porphyritic chondrules are 21–86 K h^{-1} for peak temperatures of 1623–1673 K. These cooling rates are in good agreement with experiments from Wick and Jones (2012) and other in situ measurements of cooling rates of type I chondrules using Cu-Ga zoning profiles in Acfer 097 metal (Humayun 2012) and pyroxene exsolution (Weinbruch and Müller 1995; Cuvillier et al. 2014) in other CR, CV, and CM chondrites. These results confirm a formation of type I porphyritic chondrules in CCs during similar high-temperature events.

The X-wind model implies cooling rates and peak temperatures that are too low, while the lightning model implies cooling rates that are too high compared with the empirical constraints obtained from Renazzo and Acfer 097 metal grains. The cooling rates obtained for equatorial sections of metal grain are consistent with those predicted by chondrule formation in the shock wave and impact-generated plume models. However, only the shock wave models are fully consistent with our results considering the range of peak temperatures reported here and the relationship with the associated cooling rates. In terms of thermal evolution, shock waves thus appear to be the most plausible high-temperature events for the origin of chondrules.

The ubiquitous depletions and the lack of corresponding excesses in compatible elements (e.g., Re, Os, Ir) in the metal grains investigated, with one exception showing solid metal-liquid metal fractionation, are consistent with a formation of metal in a dust-rich environment under high total pressures. However, the CR metal grains investigated here do not display the chemical characteristics of CB metal, which formed by condensation from a high-pressure impact vapor plume. Although cooling rate/temperature pairs calculated here strongly suggest a formation caused by shock waves, the chemical compositions are consistent with the splashing model for CR metal. In an expanding plume, a spray of melted metal and silicate droplets cooled and re-accreted to form chondrules. After the metal droplets solidified, recondensation of volatile elements (Cu, Ga, Ge, and Au) from the ambient gas took place on the surfaces of the solid metal grains, which were subsequently re-accreted within partially molten silicate chondrules. In terms of cooling rates, it is unfortunately not possible to fully test the splashing model because numerical modeling of droplet cooling rates in such impact plumes is lacking.

Acknowledgments—We thank Miguel Garcia-Sanz and Patricia Wils for providing CT scans produced using the AST-RX computed tomography facility (UMS 2700

CNRS-MNHN, Paris). We are also very grateful to Rhian H. Jones, Johan Villeneuve, and the AE Edward R. D. Scott for very constructive reviews and helpful comments, which led to major improvements to this manuscript. This study was supported by the ANR program THEODULE and by the NASA Cosmochemistry Program (NNX13AI06G).

Editorial Handling—Dr. Edward Scott

REFERENCES

Alexander C. M. O'D. and Ebel D. S. 2012. Questions, questions: Can the contradictions between the petrologic, isotopic, thermodynamic, and astrophysical constraints on chondrule formation be resolved? *Meteoritics & Planetary Science* 47:1–19.

Alexander C. M. O'D., Grossman J. N., Ebel D. S., and Ciesla F. J. 2008. The formation conditions of chondrules and chondrites. *Science* 320:1617–1619.

Asimow P. D. and Ghiorso M. S. 1998. Algorithmic modifications extending MELTS to calculate subsolidus phase relations. *American Mineralogist* 83:1127–1132.

Asphaug E., Martin J., and Movshovitz N. 2011. Chondrule formation during planetesimal accretion. *Earth and Planetary Science Letters* 308:369–379.

Campbell A. J. and Humayun M. 1999. Trace element microanalysis in iron meteorites by laser ablation ICPMS. *Analytical Chemistry* 71:939–946.

Campbell A. J., Humayun M., and Weisberg M. K. 2002. Siderophile element constraints on the formation of metal in the metal-rich chondrites Bencubbin, Weatherford, and Gujba. *Geochimica et Cosmochimica Acta* 66:647–660.

Chaumard N., Humayun M., Zanda B., and Hewins R. H. 2014. Igneous differentiation preserved in a large isolated metal grain from the Renazzo CR2 chondrite (abstract #2469). 45th Lunar and Planetary Science Conference. CD-ROM.

Ciesla F. J. and Hood L. L. 2002. The nebular shock wave model for chondrule formation: Shock processing in a particle-gas suspension. *Icarus* 158:281–293.

Ciesla F. J., Hood L. L., and Weidenschilling S. J. 2004. Evaluating planetesimal bow shocks as sites for chondrule formation. *Meteoritics & Planetary Science* 39:1809–1821.

Connolly H. C. Jr., Huss G. R., and Wasserburg G. J. 2001. On the formation of Fe-Ni metal in Renazzo-like carbonaceous chondrites. *Geochimica et Cosmochimica Acta* 65:4567–4588.

Connolly H. C. Jr., Desch S. J., Ash R. D., and Jones R. H. 2006. Transient heating events in the protoplanetary nebula. In *Meteorites and the early solar system II*, edited by Lauretta D. and McSween H. Y. Jr. Tucson, Arizona: The University of Arizona Press. pp. 383–397.

Cuvillier P., Chaumard N., Leroux H., Zanda B., Hewins R. H., Jacob D., and Devouard B. 2014. A TEM study of exsolution in Ca-rich pyroxenes from the Paris meteorite: Determination of type I chondrule cooling rates (abstract # 1711). 45th Lunar and Planetary Science Conference. CD-ROM.

DeHart J. M. and Lofgren G. E. 1996. Experimental studies of group A1 chondrules. *Geochimica et Cosmochimica Acta* 60:2233–2242.

Desch S. J. and Connolly H. C. Jr. 2002. A model of thermal processing of particles in solar nebula shocks: Application to the cooling rates of chondrules. *Meteoritics & Planetary Science* 37:183–207.

Desch S. J. and Cuzzi J. N. 2000. The generation of lightning in the solar nebula. *Icarus* 143:87–105.

Desch S. J., Morris M. A., Connolly H. C., and Boss A. P. 2010. A critical examination of the X-wind model for chondrule and calcium-rich, aluminum-rich inclusion formation and radionuclide production. *The Astrophysical Journal* 725:692–711.

Desch S. J., Morris M. A., Connolly H. C. Jr., and Boss A. P. 2012. The importance of experiments: Constraints on chondrule formation models. *Meteoritics & Planetary Science* 47:1139–1156.

Ebel D. S. 2006. Condensation of rocky material in astrophysical environments. In *Meteorites and the early solar system II*, edited by Lauretta D. S. and McSween H. Y. Jr. Tucson, Arizona: The University of Arizona Press. pp. 253–277.

Ebel D. S. and Grossman L. 2000. Condensation in dust-enriched systems. *Geochimica et Cosmochimica Acta* 64:339–366.

Fedkin A. V. and Grossman L. 2013. Vapor saturation of sodium: Key to unlocking the origin of chondrules. *Geochimica et Cosmochimica Acta* 112:226–250.

Fedkin A. V., Grossman L., Ciesla F. J., and Simon S. B. 2012. Mineralogical and isotopic constraints on chondrule formation from shock wave thermal histories. *Geochimica et Cosmochimica Acta* 87:81–116.

Fedkin A. V., Grossman L., Humayun M., Simon S. B., and Campbell A. J. 2015. Condensates from vapor made by impacts between metal-silicate-rich bodies: Comparison with metal and chondrules in CB chondrites. *Geochimica et Cosmochimica Acta* 164:236–261.

Gaboardi M. and Humayun M. 2009. Elemental fractionation during LA-ICP-MS analysis of silicate glasses: Implications for matrix-independent standardization. *Journal of Analytical Atomic Spectrometry* 24:1188–1197.

Ghiorso M. S. and Sack R. O. 1995. Chemical mass transfer in magmatic processes. IV. A revised and internally consistent thermodynamic model for the interpolation and extrapolation of liquid-solid equilibria in magmatic systems at elevated temperatures and pressures. *Contributions to Mineralogy and Petrology* 119:197–212.

Goldstein J. I., Hannemann R. E., and Ogilvie R. E. 1965. Diffusion in the Fe-Ni system at 1 atm and 40 kb pressure. *Transactions of the Metallurgical Society of AIME* 233:812–820.

Grossman J. N. and Wasson J. T. 1985. The origin and history of the metal and sulfide components of chondrules. *Geochimica et Cosmochimica Acta* 49:925–939.

Harju E. R., Rubin A. E., Ahn I., Choi B.-G., Ziegler K., and Wasson J. T. 2014. Progressive aqueous alteration of CR carbonaceous chondrites. *Geochimica et Cosmochimica Acta* 139:267–292.

Hewins R. H. 1997. Chondrules. *Annual Review of Earth and Planetary Sciences* 25:61–83.

Hewins R. H. and Zanda B. 2012. Chondrules: Precursors and interactions with the nebular gas. *Meteoritics & Planetary Science* 47:1120–1138.

Hewins R. H., Connolly H. C. Jr., Lofgren G. E., and Libourel G. 2005. Experimental constraints on chondrule formation. In *Chondrites and the protoplanetary disk*, edited by Krot A. N., Scott E. R. D., and Reipurth B. San Francisco, California: Astronomical Society of the Pacific. pp. 286–316.

Hewins R. H., Ganguly J., and Mariani E. 2009. Diffusion modeling of cooling rates of relict olivine in Semarkona chondrules (abstract #1513). 40th Lunar and Planetary Science Conference. CD-ROM.

Hewins R. H., Zanda B., and Bendersky C. 2012. Evaporation and recondensation of sodium in Semarkona type II chondrules. *Geochimica et Cosmochimica Acta* 78:1–17.

Hood L. L. 1998. Thermal processing of chondrule and CAI precursors in planetesimal bow shocks. *Meteoritics & Planetary Science* 33:97–107.

Hood L. L., Ciesla F. J., Artemieva N. A., Marzari F., and Weidenschilling S. J. 2009. Nebular shock waves generated by planetesimals passing through Jovian resonances: Possible sites for chondrule formation. *Meteoritics & Planetary Science* 44:327–342.

Hood L. L., Ciesla F. J., and Weidenschilling S. J. 2005. Chondrule formation in planetesimal bow shocks: Heating and cooling rates. In *Chondrites and the protoplanetary disk*, edited by Krot A. N., Scott E. R. D., and Reipurth B. San Francisco, California: Astronomical Society of the Pacific. pp. 873–882.

Hood L. L. and Horanyi M. 1991. Gas dynamic heating of chondrule precursor grains in the solar nebula. *Icarus* 93:259–269.

Humayun M. 2012. Chondrule cooling rates inferred from diffusive profiles in metal lumps from the Acfer 097 CR2 chondrite. *Meteoritics & Planetary Science* 47:1191–1208.

Humayun M., Campbell A. J., Zanda B., and Bourot-Denise M. 2002. Formation of Renazzo chondrule metal inferred from siderophile elements (abstract #1965). 33rd Lunar and Planetary Science Conference. CD-ROM.

Humayun M., Simon S. B., and Grossman L. 2007. Tungsten and hafnium distribution in calcium-aluminum inclusions (CAIs) from Allende and Efremovka. *Geochimica et Cosmochimica Acta* 71:4609–4627.

Humayun M., Connolly H. C., Rubin A. E., and Wasson J. T. 2010. Elemental distribution in metal from the CR chondrites Acfer 059 and PCA 91082 (abstract #1840). 41st Lunar and Planetary Science Conference. CD-ROM.

Jacquet E. and Thompson C. 2014. Chondrule destruction in nebular shocks. *The Astrophysical Journal* 797:30.

Johnson B. C., Minton D. A., Melosh H. J., and Zuber M. T. 2015. Impact jetting as the origin of chondrules. *Nature* 517:339–341.

Jones R. H. 1990. Petrology and mineralogy of type II, FeO- rich, chondrules in Semarkona (LL3.0): Origin by closed-system fractional crystallization, with evidence for supercooling. *Geochimica et Cosmochimica Acta* 54:1785–1802.

Jones R. H. 1994. Petrology of FeO-poor, porphyritic pyroxene chondrules in the Semarkona chondrite. *Geochimica et Cosmochimica Acta* 58:5325–5340.

Jones R. H. 2012. Petrographic constraints on the diversity of chondrule reservoirs in the protoplanetary disk. *Meteoritics & Planetary Science* 47:1176–1190.

Jones R. H. 2014. A primitive oxygen isotope reservoir for chondrules from CR chondrites. *Meteoritics & Planetary Science* 47:1176–1190.

Jones R. H. and Lofgren G. E. 1993. A comparison of FeO-rich porphyritic olivine chondrules in unequilibrated chondrites and experimental analogues. *Meteoritics* 28:213–221.

Kong P. and Palme H. 1999. Compositional and genetic relationship between chondrules, chondrule rims, metal, and matrix in the Renazzo chondrite. *Geochimica et Cosmochimica Acta* 63:3673–3682.

Kong P., Ebihara M., and Palme H. 1999. Distribution of siderophile elements in CR chondrites: Evidences for evaporation and recondensation during chondrule formation. *Geochimica et Cosmochimica Acta* 63:2637–2652.

Krot A. N., Meibom A., Weisberg M. K., and Keil K. 2002. The CR chondrite clan: Implications for early solar system processes. *Meteoritics & Planetary Science* 37:1451–1490.

Krot A. N., Amelin Y., Cassen P., and Meibom A. 2005. Young chondrules in CB chondrites from a giant impact in the early solar system. *Nature* 436:989–992.

Le Guillou C., Changela H., and Brearley A. 2015. Widespread oxidized and hydrated amorphous silicates in CR chondrites matrices: Implications for alteration conditions and H_2 degassing of asteroids. *Earth and Planetary Science Letters* 420:162–173.

Lofgren G. E. 1996. A dynamic crystallization model for chondrule melts. In *Chondrules and the protoplanetary disk*, edited by Hewins R. H., Jones R. H., and Scott E. R. D. Cambridge, UK: Cambridge University Press. pp. 187–196.

Miyamoto M., Mikouchi T., and Jones R. H. 2009. Cooling rates of porphyritic olivine chondrules in the Semarkona (LL3.00) ordinary chondrite: A model for diffusional equilibration of olivine during fractional crystallization. *Meteoritics & Planetary Science* 44:521–530.

Morfill G., Spruit H., and Levy E. H. 1993. Physical processes and conditions associated with the formation of protoplanetary disks. In *Protostars and planets III*, edited by Levy E. H. and Lunine J. I. Tucson, Arizona: The University of Arizona Press. pp. 939–978.

Morlok A. and Libourel G. 2013. Aqueous alteration in CR chondrites: Meteorite parent body processes as analogue for long-term corrosion processes relevant for nuclear waste disposal. *Geochimica et Cosmochimica Acta* 103:76–103.

Morris M. A., Boley A. C., Desch S. J., and Athanassiadou T. 2012. Chondrule formation in bow shocks around eccentric planetary embryos. *The Astrophysical Journal* 752:27.

Morris M. A. and Desch S. J. 2010. Thermal histories of chondrules in solar nebula shocks. *The Astrophysical Journal* 722:1474–1494.

Oulton J., Humayun M., Fedkin A., and Grossman L. 2016. Chemical evidence for differentiation, evaporation and recondensation from silicate clasts in Gujba. *Geochimica et Cosmochimica Acta* 177:254–274.

Pilipp W., Hartquist T. W., Morfill G. E., and Levy E. H. 1998. Chondrule formation by lightning in the Protosolar Nebula? *Astronomy & Astrophysics* 331:121–146.

Radomsky P. M. and Hewins R. H. 1990. Formation conditions of pyroxene-olivine and magnesian olivine chondrules. *Geochimica et Cosmochimica Acta* 54:3475–3490.

Righter K., Campbell A. J., and Humayun M. 2005. Diffusion of trace elements in FeNi metal: Applications to zoned metal grains in chondrites. *Geochimica et Cosmochimica Acta* 69:3145–3158.

Rubin A. E. 1997. Mineralogy of meteorite groups. *Meteoritics & Planetary Science* 32:231–247.

Sanders I. S. 1996. A chondrule-forming scenario involving molten planetesimals. In *Chondrules and the protoplanetary disk*, edited by Hewins R. H., Jones R. H., and Scott E. R. D. Cambridge, UK: Cambridge University Press. pp. 327–334.

Sanders I. S. and Scott E. D. 2012. The origin of chondrules and chondrites: Debris from low-velocity impacts between molten planetesimals? *Meteoritics & Planetary Science* 47:2170–2192.

Sanders I. S. and Taylor G. J. 2005. Implications of ^{26}Al in nebular dust: Formation of chondrules by disruption of molten planetesimals. In *Chondrites and the protoplanetary disk*, edited by Krot A. N., Scott E. R. D., and Reipurth B. San Francisco, California: Astronomical Society of the Pacific. pp. 821–838.

Schrader D. L., Davidson J., Greenwood R. C., Franchi I. A., and Gibson J. M. 2014. A water-ice rich minor body from the early solar system: The CR chondrite parent asteroid. *Earth and Planetary Science Letters* 407:48–60.

Sears D. W. G., Huang S., and Benoit P. H. 1996. Open-system behaviour during chondrule formation. In *Chondrules and the protoplanetary disk*, edited by Hewins R. H., Jones R. H., and Scott E. R. D. Cambridge, UK: Cambridge University Press. pp. 221–231.

Shu F. H., Shang H., Gounelle M., Glassgold A. E., and Lee T. 2001. The origin of chondrules and refractory inclusions in chondritic meteorites. *The Astrophysical Journal* 548:1029–1050.

Shu F. H., Shang H., and Lee T. 1996. Toward an astrophysical theory of chondrites. *Science* 271:1545–1552.

Sorby H. C. 1877. On the structure and origin of meteorites. *Nature* 15:495–498.

Stammler S. M. and Dullemond C. P. 2014. A critical analysis of shock models for chondrule formation. *Icarus* 242:1–10.

Tenner T. J., Nakashima D., Ushikubo T., Kita N. T., and Weisberg M. K. 2015. Oxygen isotope ratios of FeO-poor chondrules in CR3 chondrites: Influence of dust enrichment and H_2O during chondrule formation. *Geochimica et Cosmochimica Acta* 148:228–250.

Uesugi M., Sekiya M., and Nakamura T. 2008. Kinetic stability of a melted iron globule during chondrule formation. I. Non-rotating model. *Meteoritics & Planetary Science* 43:717–730.

Villeneuve J., Libourel G., and Soulié C. 2015. Relationships between type I and type II chondrules: Implications on chondrule formation processes. *Geochimica et Cosmochimica Acta* 160:277–305.

Wasson J. T. and Rubin A. E. 2009. Composition of matrix in the CR chondrite LAP 02342. *Geochimica et Cosmochimica Acta* 73:1436–1460.

Wasson J. T. and Rubin A. E. 2010. Metal in CR chondrites. *Geochimica et Cosmochimica Acta* 74:2212–2230.

Watson H. C. and Watson E. B. 2003. Siderophile trace element diffusion in Fe-Ni alloys. *Physics of the Earth and Planetary Interiors* 139:65–75.

Weidenschilling S. J., Marzari F., and Hood L. L. 1998. The origin of chondrules at Jovian resonances. *Science* 279:681–684.

Weinbruch S. and Müller W. F. 1995. Constraints on the cooling rates of chondrules from the microstructure of clinopyroxene and plagioclase. *Geochimica et Cosmochimica Acta* 59:3221–3230.

Weisberg M. K., Prinz M., Clayton R. N., and Mayeda T. 1993. The CR (Renazzo-type) carbonaceous chondrite group and its implications. *Geochimica et Cosmochimica Acta* 57:1567–1586.

Wick M. J. and Jones R. H. 2012. Formation conditions of plagioclase-bearing type I chondrules in CO chondrites: A study of natural samples and experimental analogs. *Geochimica et Cosmochimica Acta* 98:140–159.

Wood J. A. 1963. On the origin of chondrules and chondrites. *Icarus* 2:152–180.

Yoneda S. and Grossman L. 1995. Condensation of CaO-MgO-Al_2O_3-SiO_2 liquids from cosmic gases. *Geochimica et Cosmochimica Acta* 59:3413–3444.

Zanda B. 2004. Chondrules. *Earth and Planetary Science Letters* 224:1–17.

Zanda B., Bourot-Denise M., Hewins R. H., Cohen B. A., Delaney J. S., Humayun M., and Campbell A. J. 2002. Accretion textures, iron evaporation and re-condensation in Renazzo chondrules (abstract #1852). 33rd Lunar and Planetary Science Conference. CD-ROM.

Zanda B., Hewins R. H., Bourot-Denise M., Bland P. A., and Albarède F. 2006. Formation of solar nebula reservoirs by mixing chondritic components. *Earth and Planetary Science Letters* 248:650–660.